The Astronomical Journal, 166:200 (33pp), 2023 November https://doi.org/10.3847/1538-3881/acfc47

Observational Constraints on Close Binary Star Evolution. I. Putative Contact Binaries with Long Periods and High Mass Ratios

Evan M. Cook and Henry A. Kobulnicky
University of Wyoming, 1000 E University Avenue, Laramie, WY 82071, USA; ecook16@uwyo.edu
Received 2023 August 14; revised 2023 September 18; accepted 2023 September 20; published 2023 October 18

Abstract

Evolutionary and structural models for contact binary stars make quantitative predictions about the distribution of systems in the mass ratio (q)–orbital period (P) plane. Specifically, contact binaries containing primaries with convective envelopes are predicted to be absent at mass ratios larger than a critical threshold that is a function of orbital period and total mass. We test this prediction by characterizing candidate contact binaries that appear to have mass ratios in violation of this threshold. We obtained quadrature-phase echelle spectra ($R \approx 31{,}000$) for 18 close binaries (0.65 day $< P <$ 2.00 days) in the Kepler field, from which we extracted radial velocity profiles for each system. Use of a joint Markov Chain Monte Carlo fitting routine on the Kepler light curves and the radial velocity profiles allows us to retrieve all fundamental system and component parameters. Of the 18 systems, only one is a contact binary, and both components likely have radiative—not convective—envelopes. The 17 remaining systems are detached binaries (eight) or semidetached binaries (four) with ellipsoidal variations, rotating variables (four), or pulsating variables (one). Therefore, none of the systems are in violation of the theoretical mass ratio thresholds for low-mass contact binaries. The 12 noncontact binaries follow a T_2/T_1–q relation significantly weaker than expected for main-sequence components, suggesting radiative heating of the secondaries. Most of the secondaries have radii larger than main-sequence expectations, a possible consequence of heating. Four secondaries fill their Roche lobes, while none of the primaries do, possibly indicating prior mass-ratio reversal.

Unified Astronomy Thesaurus concepts: Contact binary stars (297); Close binary stars (254); Multiple star evolution (2153); Stellar evolutionary tracks (1600); Stellar evolutionary models (2046); Ellipsoidal variable stars (455)

1. Introduction

In the solar neighborhood, approximately 35% of stellar systems are binaries (Reid & Gizis 1997). For Sun-like stars specifically, almost 50% are in binary or higher-order systems (Raghavan et al. 2010), and this binary fraction increases steeply with stellar mass (Chini et al. 2012). Approximately 0.2% of F, G, and K main-sequence stars orbit so closely that they share a convective atmospheric envelope (Lucy 1968; Rucinski 2006), earning them the name "contact binaries" (Kuiper 1941). They are also called W Ursae Majoris stars (W UMas) after their archetype (Muller & Kempf 1903), and they are the most common type of eclipsing variables (Shapley 1948). In many ways, contact binaries are very simple. They are composed of stars similar to the Sun, and they have circular orbits (Binnendijk 1970; Duquennoy & Mayor 1991), equal rotational and orbital periods, and approximately equal surface temperatures owing to their common convective envelopes (Yakut & Eggleton 2005). However, their apparent simplicity belies the complexity of their evolutionary histories, described by Eggleton (2012) to be "one of the two great unsolved problems of stellar astrophysics."

Forming a contact binary requires two stages. The first stage involves creating close binaries from more widely separated binaries. This is accomplished by one or both of two mechanisms: Kozai–Lidov Cycles with Tidal Friction (KLCTF; Kiseleva et al. 1998; Fabrycky & Tremaine 2007) and protostellar disk interactions (Bonnell & Bate 2005; Tokovinin & Moe 2020). Kozai–Lidov Cycles are oscillations in the eccentricity of a binary caused by a third star on a more distant, mutually inclined orbit. When the inner two stars are at periastron, they interact tidally, dissipating energy and shrinking the semimajor axis. This model does not make any predictions about the distribution of initial mass ratios for contact binaries (Kiseleva et al. 1998; Fabrycky & Tremaine 2007). Alternatively, disk interactions between neighboring protostars can also produce close binaries. As the protostars migrate inward, a circumbinary disk is eventually formed, which promotes further inward migration of the two protostars. This model predicts that the distribution of mass ratios for close binaries—and thus newborn contact binaries—should be mostly uniform, but with a pileup of "twins," systems with mass ratios near unity (Tokovinin & Moe 2020).

Eventually, KLCTF and/or disk interactions will shrink the orbit enough that tidal evolution in concert with magnetic braking can take over—the second stage. According to the Darwin (1879) weak tidal friction model, close binaries will evolve toward smaller, circular orbits and synchronous, coplanar spins (Hut 1981). Simultaneous with this tidal evolution, magnetic braking steals angular momentum from the stars' rotations (Schatzman 1962). However, because the stars are constrained to rotate at the same rate they orbit, angular momentum is indirectly stolen from the stars' orbits, bringing the stars even closer together. This forces the stars to rotate faster to remain synchronized (Huang 1966). More rapidly rotating stars have stronger magnetic fields, so this is a runaway process, albeit a very slow one. Theoretical estimates for the time required for magnetic braking to bring two main-

sequence stars into contact range from about a million years to over 10 Gyr, depending on the initial orbital period and the masses of the stars involved (Jiang et al. 2014).

Once contact is achieved, the evolution of the system depends on the initial masses and the mass ratio. If the mass ratio is sufficiently extreme, the pair will merge upon coming into contact (Jiang et al. 2012). However, if the pair survives, the more massive star loses mass to the secondary until the system reaches a dynamical equilibrium. If the mass ratio is near unity, however, Flannery (1976) found that it will still be thermally unstable, and will evolve below $q \equiv M_2/M_1 \approx 0.8$ on a timescale of about 10 Myr. Although he computed just one cycle for just one case (due to computational limitations), Flannery (1976) concluded that systems of all mass ratios undergo ongoing cycles of thermal instabilities (i.e., thermal relaxation oscillations). This conclusion has been widely adopted by others since (e.g., Yakut & Eggleton 2005, and references therein). By contrast, Molnar et al. (2022, hereafter M22) used MESA stellar evolutionary models (Paxton et al. 2011) with mass transfer modifications to show that at $q \lesssim 0.8$ there exists a set of thermally *stable* evolutionary tracks along which systems evolve monotonically toward more extreme mass ratios and longer orbital periods. The evolutionary tracks are best visualized in the mass ratio versus orbital period plane (q–P plane), as in Figure 64 from Kobulnicky et al. (2022, hereafter K22). These tracks constitute testable predictions for the distribution of contact binaries in the q–P plane.

Models for the evolution of contact binaries (e.g., Webbink 1976; Gazeas & Stępień 2008; Molnar et al. 2022), coupled with the standard mass–radius relationship for main-sequence stars, predict that high-mass-ratio, long-period contact binaries should not exist, at least not with main-sequence F-, G-, or K-type primaries. The upper-right quadrant of the q–P plane should be devoid of contact binaries with main-sequence primaries, because of the requirements of Roche geometry, basic orbital dynamics, and conservation of angular momentum. A long-period binary must have some combination of a large semimajor axis or a low mass. In either case, the components cannot fill their Roche lobes unless the primary is evolved. K22 performed a Bayesian analysis on the light curves of a complete, unbiased sample of 783 Kepler short-period ($P < 2$ days) eclipsing or ellipsoidal binaries, allowing them to derive probabilistic values for q. Their Figure 64 shows the results in the q–P plane along with the M22 evolutionary tracks. The figure shows ∼20 systems at longer periods ($P \gtrsim 0.65$ day) and high mass ratios ($q \gtrsim 0.5$), all lying above the model tracks, but they were unable to determine on the basis of the light curves whether they have contact or detached geometries, so they labeled these as ambiguous. On the basis of the model tracks, we would expect this region of the diagram to contain only detached binaries, rare contact systems containing an evolved primary, or single-star variables mistakenly identified as eclipsing or ellipsoidal binaries.

A second prediction arising from these models entails a lower limit on q. The Hut (1981) application of the Darwin (1879) weak friction model specifies a clear instability criterion for contact binaries with low mass ratios: $L_{\rm spin} > 0.25 L_{\rm total}$—the Darwin instability criterion. Theoretical attempts to define this lower limit span a large range from 0.07–0.09 (Rasio 1995; Li & Zhang 2006; Arbutina 2007, 2009) to 0.25 (Wadhwa et al. 2021). A rigorous determination of the lower limit on q from the above criterion requires a knowledge of the moment of inertia coefficients (k) of the binary components over the evolutionary lifetime of the primary. One reason for the large range of theoretical determinations for $q_{\rm min}$ is that k is also affected by whether the star is radiative (typically A-type binaries, more-massive primaries) or convective (W-type binaries, less-massive primaries). M22 used MESA stellar evolutionary models with mass transfer modifications to calculate k as a function of evolutionary state for contact binaries with initial primary mass $\leqslant 1.3\,M_\odot$ (i.e., those with convective envelopes, approximately F8 and later). Their calculations resulted in a theoretical lower limit on mass ratio that is a function of orbital period, ranging from $q \approx 0.05$ below $P \approx 0.8$ day to $q \approx 0.15$ above $P \approx 1.6$ days. No stable contact binaries should exist below this limit. Indeed, K22 found no contact systems that definitively violate this lower limit, but they do find some having 1σ error bars that straddle it. Such systems merit precise spectroscopic measurements of q that provide strong constraints on $q_{\rm min}$ as a function of orbital period and total mass.

Models of contact binary evolution also predict that contact systems with q near unity should be rare on account of the thermal instability that rapidly drives them toward lower q (Molnar et al. 2022). The protostellar disk fragmentation model of Tokovinin & Moe (2020) predicts that close detached binaries have a flat distribution of q, but with an excess of twins. This excess is larger for systems with shorter periods, implying that there should be an excess of twins among newborn contact binaries. The observed distribution of contact binaries features a peak near $q \lesssim 0.3$ and a paucity of systems near $q = 1$ (Latković et al. 2021; Kobulnicky et al. 2022; Pešta & Pejcha 2022), supporting the idea that those latter systems are unstable. Still, K22 found that 49 of 699 systems (7%) have $q > 0.8$, and this fraction diminishes to 6 of 178 (3%) for probable contact systems. A comparison of the ∼10 Myr timescale to evolve below $q \approx 0.8$ and the lifetime of contact binaries—roughly between 1 and 10 Gyr—predicts that only a very small fraction (between 0.1% and 1%) of contact binaries should exist with mass ratios near unity. This tension could be resolved in a number of ways. Either the systems that K22 found above $q = 0.8$ could contain systems that are not contact binaries, the Kepler sample could be biased toward younger recently formed stars and star clusters such that contact binaries are overrepresented, the lifetime of contact binaries could be shorter than the commonly accepted several billion years, or theoretical investigations of the region above $q \approx 0.8$ could have underestimated the timescale of the instability. Spectroscopic observations of putative contact systems with $q \gtrsim 0.8$ are needed to pinpoint the cause of the discrepancy.

Finally, the evolutionary models of M22 predict that the low-q short-P corner of the q–P plane is populated exclusively by systems having small total masses, $M_{\rm tot} \lesssim 1.4\,M_\odot$. These systems evolve almost horizontally and very slowly in the q–P plane over >9 Gyr, starting at periods $P \approx 0.25$ day and approaching the limiting mass ratio of $q \approx 0.05$ at periods of ≈0.5 day. Systems having larger total masses follow quasi-parallel tracks starting at larger q and evolving toward smaller q and larger P over much shorter timescales—as short as 2 Gyr in the case of systems with $M_{\rm tot} = 1.9\,M_{\rm sol}$. More-massive systems may approach periods of over 2 days as they reach the Darwin instability limit. Therefore, the 1.4 days period of V1309 Sco at the time of merger—initially deemed outside the

accepted range of W UMa periods (Tylenda et al. 2011)—is consistent with the evolutionary endpoint of an $M_{\rm tot} = 1.7\,M_{\odot}$ to $1.9\,M_{\odot}$ system with an initial $q \gtrsim 0.6$. Although K22 were not able to measure total system masses from light curves alone, the distribution in the q–P plane (their Figure 64) shows a preponderance of systems at short periods $P \approx 0.3$ day and moderate mass ratios $q \approx 0.3$, qualitatively consistent with the predicted slow evolution over the first 2–5 Gyr for typical Galactic populations of contact binaries. Reliable measurements of mass ratios and total system masses would enable a meaningful quantitative test of the M22 evolutionary tracks.

In this paper we present a joint analysis of new multiepoch echelle $R \approx 31{,}000$ spectroscopy and Kepler photometry for 18 systems drawn from the long-P ($P > 0.65$ day) high-q ($q > 0.5$) corner of the q–P plane (Kobulnicky et al. 2022). Our objective is to determine the nature of these candidate contact binaries inhabiting a region of the q–P plane that, theoretically, should be inaccessible to W UMa systems. When combined with photometry, spectroscopic data break degeneracies in photometric-only models and allow calculation of direct mass ratios, individual component masses, and total system masses. Section 2 covers the sample selection process and spectroscopic observations, data reductions, and computation of the broadening function (Rucinski 1999; i.e., the light-weighted velocity profile of the system) at each of two quadrature phases. Section 3 describes the methods by which we conduct a joint Bayesian analysis of spectroscopic and photometric data that yield a full set of system parameters. Section 4 presents these parameters along with physical diagnoses of the natures and geometries of the individual targets. In Section 5 we analyze higher level trends in the results, we compare our results to those of K22, and we discuss implications of our results for the M22 evolutionary tracks. Section 6 lays out our conclusions. Throughout this paper, we follow the lead of investigations like Yakut & Eggleton (2005) and Gazeas & Stępień (2008) in defining the primary star M_1 in a close binary system to be the currently more massive component. This greatly reduces confusion when discussing orbital dynamics and evolutionary scenarios. We have the benefit of using this definition, because the spectra allow us to unambiguously determine which component is more massive.

2. Spectroscopic Observations

2.1. Sample Selection

We selected targets for spectroscopic follow-up from the K22 sample of 783 Kepler binaries on the basis of having orbital periods $P > 0.65$ day and mass ratios indicated by the light-curve analysis $q > 0.5$. Additionally, we limited the sample to systems brighter than 14th magnitude in the Kepler Kp band. Applying these conditions yielded the current sample of 18 putative close binaries listed in Table 1. For each of our targets, column 1 gives the Kepler Input Catalog (KIC) number, columns 2 and 3 give the R.A. and decl., column 4 gives the magnitude in the Kepler Kp band, columns 5 and 6 give the orbital period P and the reference time (t_0) for phase 0 from the Kepler Input Catalog (Brown et al. 2011), column 7 gives the effective temperature, and column 8 gives the inverse parallax distances from Gaia DR3. K22 identified all of these targets as having ambiguous geometries.

2.2. ARCES Observations and Reductions

We obtained echelle spectroscopy on the 18 putative contact binaries over 15 nights between 2022 April and 2023 July using the 3.5 m telescope at the Apache Point Observatory.[1] ARCES,[2] the Astrophysical Research Consortium Echelle Spectrograph (Wang et al. 2003) has a slit size of $1\farcs6 \times 3\farcs2$, yielding a spectral resolution $R \approx 31{,}000$ covering the range from 3200–10000 Å. Table 2 details our observations, giving times and orbital phases for exposures taken near both quadratures for each target.[3] For all but the brightest target, KIC06670812, exposure times were 600 or 900 s. Column 1 gives the KIC designation for each target, columns 2 and 4 give the Heliocentric Julian Dates of near-quadrature exposures, and columns 3 and 5 give the corresponding orbital phases.

We reduced all data in IRAF[4] (Tody 1986, 1993) following standard procedures[5] that included bias removal using the overscan region and flat-fielding using internal quartz lamps. We extracted only 32 of the 107 orders, covering the wavelength range 4805–6647 Å, the portion of the spectrum richest in spectral features and to which ARCES is most sensitive. The instrumental spectral profile at 6000 Å is well represented by a Gaussian with an FWHM of 2.35 pixels (0.184 Å, 9.2 km s^{-1}). ThAr lamp exposures yielded a wavelength calibration with an rms of 0.007 Å (0.35 km s^{-1} at 6000 Å). Analyzing nights with multiple ThAr exposures reveals typical shifts in the wavelength solution of <1 pixel (0.076 Å, 3.8 km s^{-1}). For each spectrum, we normalized and combined the orders into a single, contiguous 1D spectrum, and corrected it to the Heliocentric velocity frame. We excised the wavelength ranges 5885–5902 Å and 6275–6330 Å from the spectra to remove interstellar sodium lines and telluric features, respectively. Observations of radial velocity standards HIP 95446 and HIP 96514 (Soubiran et al. 2018) show that the mean differences between our values obtained using a model stellar template and the Gaia radial velocities for the two standards are 0.21 and 0.73 km s^{-1}, respectively, with a night-to-night dispersion of $\approx$1 km s^{-1}. Observations of the narrow-lined extreme-third-light systems V1187 Her and NSVS 2569022 taken across three different years show that the stability of the wavelength solution is precise to $\approx$0.5 km s^{-1}. For a typical G- or K-type target with a $K_p \approx 12$ mag, the final spectra have a signal-to-noise ratio of $\approx$30 in the vicinity of 6000 Å.

3. Broadening Function Analysis

3.1. The Utility of Broadening Functions

A broadening function is a powerful way to extract the velocity broadened profile of a system from spectroscopy (Rucinski 1992). Generating a broadening function requires

[1] Based on observations obtained with the Apache Point Observatory 3.5 m telescope, which is owned and operated by the Astrophysical Research Consortium.

[2] https://www.apo.nmsu.edu/arc35m/Instruments/ARCES/

[3] For systems that turned out to be rotational variables or detached, we did not always obtain data on the second quadrature.

[4] https://iraf-community.github.io/

[5] See Thorburn's (https://www.apo.nmsu.edu/arc35m/Instruments/ARCES/images/echelle_data_reduction_guide.pdf) and Kinemuchi's (http://astronomy.nmsu.edu/apo-wiki/lib/exe/fetch.php?media=wiki:arces:kinemuchi_arces_cookbook.pdf) guides for reducing ARCES data.

Table 1
Spectroscopic Targets

KIC ID	α (J2000)	δ (J2000)	Kp (mag)	P (days)	t_0 (BJD–2450000)	$T_{\rm eff}$ (K)	Dist. (kpc)
(1)	(2)	(3)	(4)	(5)	(6)	(7)	(8)
01295531	19:26:20.04	+36:55:06.10	⋯	1.686	4999.678806	6567[a]	0.712
04954113	19:55:39.26	+40:04:22.16	11.93	0.668	5001.996853	7730[b]	0.926
05196301	19:37:36.66	+40:20:14.49	13.00	1.910	4955.143163	4546[c]	0.235
05386810	19:51:41.23	+40:31:09.73	12.68	0.889	4954.086668	7395[c]	0.985
05802834	19:41:04.88	+41:01:26.80	12.21	1.092	4954.476652	6077[c]	1.158
06670812	18:57:25.36	+42:06:12.51	7.24	1.742	5002.332640[f]	6403[d]	0.107
06692340	19:28:21.60	+42:08:17.96	13.33	0.675	4954.464180[f]	6270[c]	1.446
07766185	19:44:03.94	+43:26:12.31	12.11	0.835	4954.554702	6437[a]	0.934
07884842	19:18:46.71	+43:37:33.64	9.60	1.315	4954.893014	9126[c]	0.537
07976783	19:48:43.35	+43:45:52.50	11.99	1.209	4954.862925[f]	8071[a]	1.688
07977261	19:49:11.35	+43:46:37.62	13.15	0.926	4954.341041	6910[b]	1.881
08386865	19:53:41.39	+44:19:39.86	12.02	1.258	4953.926763	9226[b]	1.274
08451777	19:53:49.03	+44:25:24.53	13.43	1.515	5000.462048	6752[a]	1.344
08452840	19:54:51.00	+44:29:04.27	12.59	1.201	4954.148064	6606[a]	1.139
08846978	20:02:43.35	+45:00:07.76	13.37	1.379	4954.873660	5680[e]	0.908
09480977	19:50:07.44	+46:01:03.30	12.30	0.871	4954.863400[f]	7357[a]	0.787
09602542	19:48:30.72	+46:12:34.93	13.89	1.463	4965.336523	7899[a]	2.611
10789421	19:14:18.56	+48:07:46.28	11.85	0.777	4953.919448	7137[a]	0.834

Notes.
[a] Frasca et al. (2016).
[b] Zhang et al. (2019).
[c] Prša et al. (2011).
[d] Casagrande et al. (2011).
[e] Qian et al. (2018).
[f] A t0 that had to be shifted half a period in order for $\phi = 0$ to occur when the more-massive star is being eclipsed.

Table 2
Times and Phases of Spectroscopic Observations

KIC ID	t_1 (HJD–2,400,000)	ϕ_1	t_2 (HJD–2,400,000)	ϕ_2
(1)	(2)	(3)	(4)	(5)
01295531	59815.7728	0.274	59826.7563	0.787
04954113	60065.7819	0.210	60135.6319	0.772
05196301	59815.7605	0.280	59877.6952	0.700
05386810	59794.7097	0.690	59697.8820	0.759
05802834	60105.6472	0.277	60105.6875	0.314
06670812	59820.6526	0.266	59697.8464	0.761
06692340	59731.8860	0.241	59697.8244	0.768
07766185	59879.7390	0.196	59826.7930	0.822
07884842	60105.6618	0.282	59815.7856	0.768
07976783	60107.7785	0.153	59820.7453	0.711
07977261	59794.7053	0.236	59697.9687	0.747
08386865	59879.5453	0.308	59877.6017	0.763
08451777	⋯	⋯	59827.7052	0.756
08452840	59697.8361	0.257	59873.7461	0.707
08846978	59697.8115	0.253	59815.7482	0.773
09480977	60107.6708	0.257	59820.6639	0.755
09602542	59827.7691	0.208	59879.7257	0.717
10789421	59794.6874	0.258	59697.9569	0.742

comparing spectra of a target with a narrow-lined template spectrum of the appropriate temperature and surface gravity. This allows for the extraction of the velocity shifts and velocity broadening of spectral features. For a close binary system, the dominant cause of spectral line broadening is stellar rotation, and the dominant cause of line shifts is stellar orbital motion. In this way, the broadening function yields both the radial velocities of the two stars and their projected rotational velocities.

Figure 1 shows two broadening functions for KIC06670812; the upper panel shows the BF corresponding to the first quadrature phase ($\phi \approx 0.25$) and the bottom panel corresponds to the second quadrature phase ($\phi \approx 0.75$). The vertical axis is intensity in arbitrary units, and the horizontal axis is Heliocentric radial velocity. The dotted line represents the instrumental profile. These broadening functions show three clear peaks, indicating a triple system composed of an inner short-period binary and a more distant, possibly unrelated tertiary. The two broad peaks labeled "1" and "2," corresponding to the inner binary, are centered near $\pm 100\,{\rm km\,s^{-1}}$, trading places from one quadrature phase to the next. The fact that they nearly trade places indicates that the velocity amplitudes of the components are similar, indicating that $q \approx 1$. The third peak corresponds to the tertiary and remains near $0\,{\rm km\,s^{-1}}$. Because both stars in the tidally locked inner binary are rotating with the same angular velocity, the width of components 1 and 2 are directly proportional to the radii of the primary and secondary stars, respectively. By contrast, component 3 is often not much wider than the instrumental profile, owing to the tertiary's relatively small rotational velocity. Therefore, we fit the inner two stars with analytical functions for rotationally broadened single stars, but we fit the tertiary with a Gaussian. The integrals of these curves represent the relative fluxes from the three stars. For a contact binary with equal-temperature components, the ratio of the components' fluxes is equal to the ratio of their projected surface areas. However, the separation between components 1 and 2 in

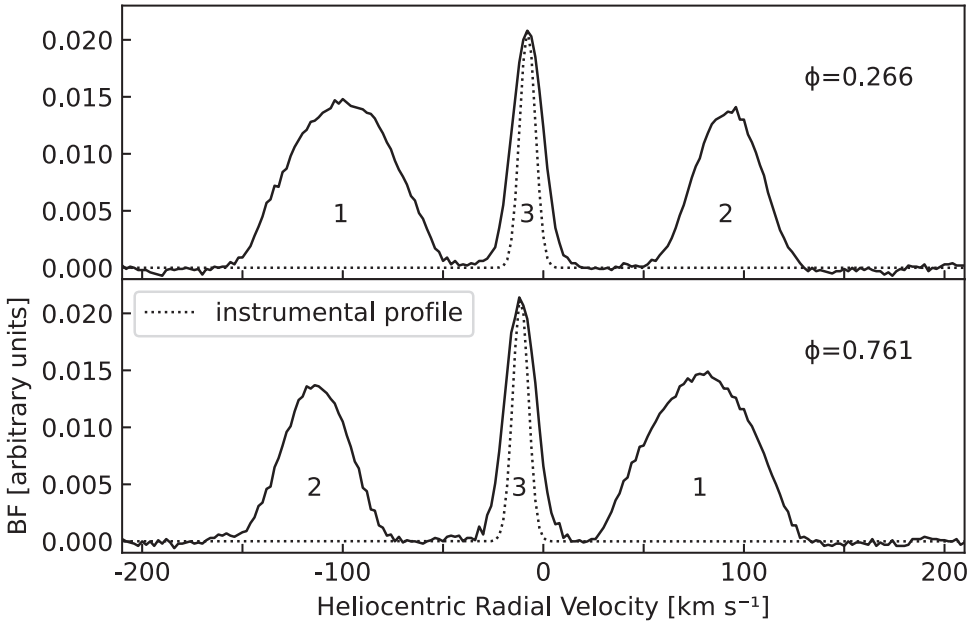

Figure 1. Broadening functions for KIC06670812. The primary, secondary, and tertiary components are labeled "1," "2," and "3," respectively, near both quadrature phases.

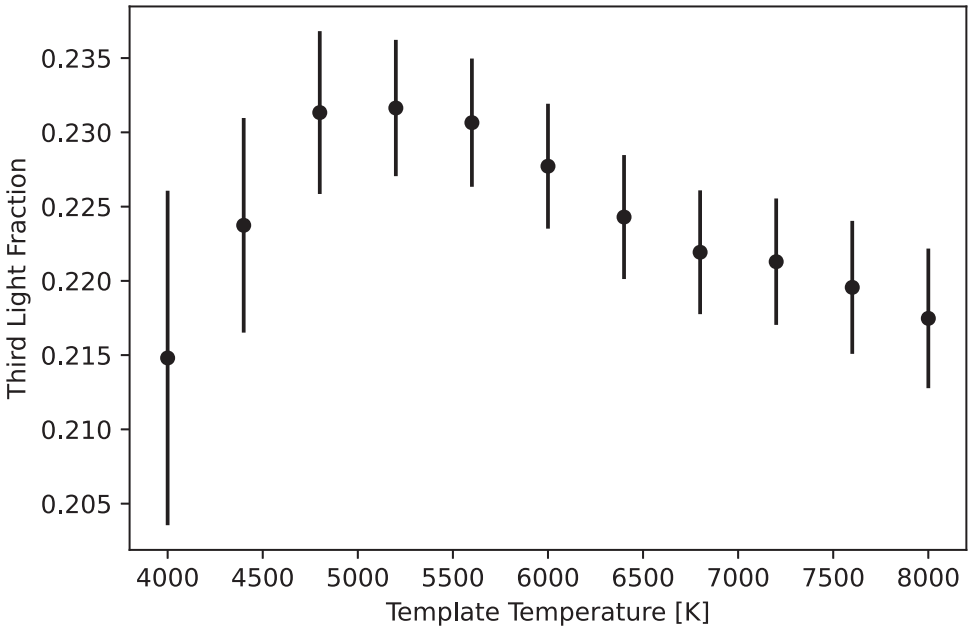

Figure 2. Third light fractions for KIC06670812 obtained from broadening functions produced using a range of stellar template temperatures.

Figure 1 indicates that KIC06670812 is a detached binary, meaning that the two binary components likely have significantly different surface temperatures.

The BF also enables a comparison between the flux of the tertiary star and the total light from the system. Assuming the choice of stellar template spectrum is equally valid for all three components, this comparison yields the third light fraction of the system. In this case, the fractional area of component 3 relative to all components is ≈0.22. When properly interpreted, the BF yields measurements of the third-light fraction ($l3$), the projected rotational and orbital velocities of each star ($v_R \sin i$ and v_{rad}, respectively), the radius ratio (R_2/R_1) and mass ratio (q) of the inner binary, the systemic radial velocity (v_0), and the radial velocity of component 3 (v_3). Given an orbital inclination derived from a light curve, the BF yields all of the relevant system physical parameters.

While the broadening function in Figure 1 does not unambiguously determine the third light fraction of the system, comparing BFs produced using a range of stellar templates places strong constraints on both the third light fraction and the temperature of the tertiary component. This is because the choice of stellar model influences the relative prominence of different components in the resulting broadening function, therefore influencing the derived third light fraction. Figure 2 plots third light fraction versus template temperature for KIC06670812 obtained from broadening functions produced using a range of stellar templates from 4000–8000 K. Figure 2 reveals that the third light fraction is greatest when using stellar

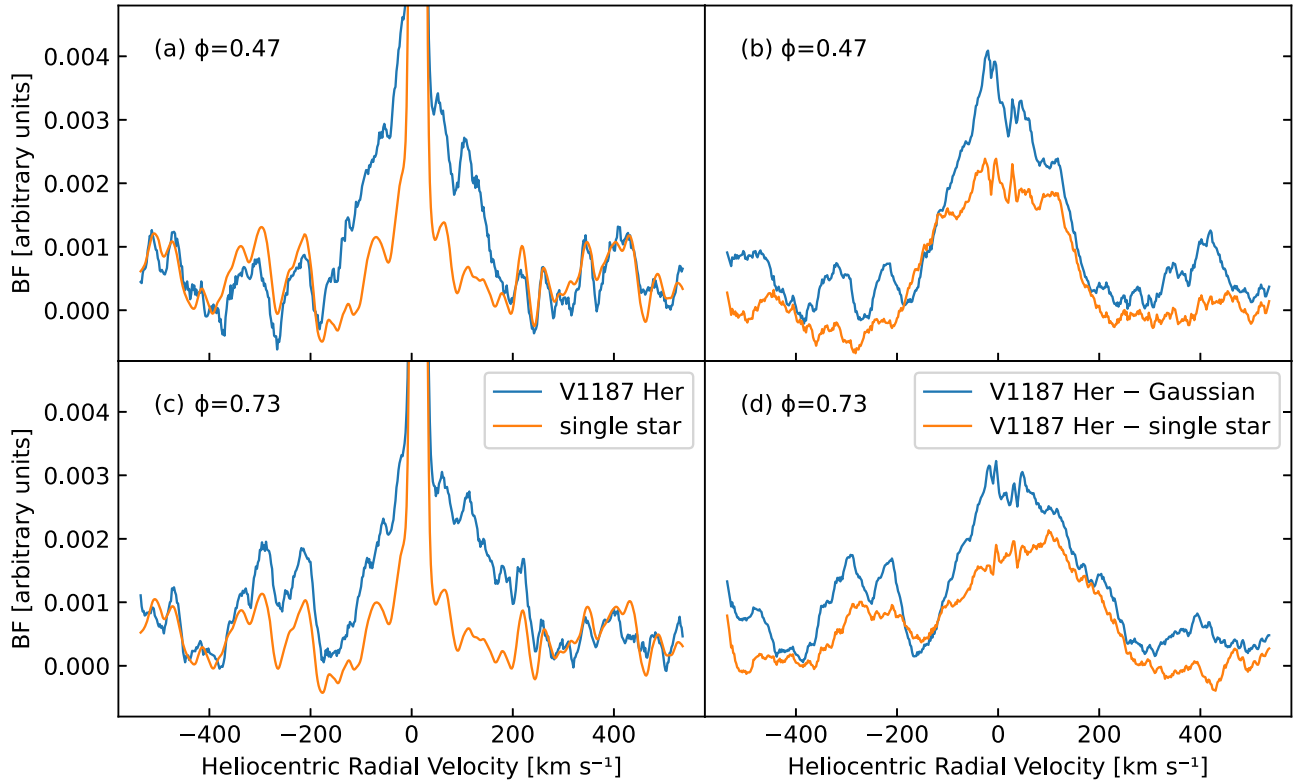

Figure 3. The extraction of extreme third light from BFs. The left two panels (a) and (c) compare the BFs corresponding to two different phases of a system containing large $l3$ (blue curves) to the BF of a slowly rotating single star (orange curves). The right two panels (b) and (d) contrast the results of subtracting a Gaussian fit to the third light (producing the blue curves) with the results of subtracting the scaled, shifted single star's BF (producing the orange curves). The latter yields a superior subtraction of third light.

templates in the temperature range 4800–5600 K, but always lies in the narrow range 0.210–0.235. A joint Bayesian fit to both the light curve (LC) and the BF (see Section 3.2) indicates that the primary and secondary components are approximately equal in temperature (≈6400 K). The fact that the third light fraction peaks when using template temperatures below 6000 K indicates that the temperature of the tertiary is indeed lower than that of either star in the inner binary. This is consistent with a third light fraction of 22%, assuming a main-sequence tertiary. In summary, even without precise knowledge of the temperatures of stellar components, broadening functions can reveal both the third light fraction and the probable temperature of the tertiary.

The BF also provides a measure of $v_R \sin i$ of third stars from their broadening functions. Figure 1 shows that the tertiary peak (solid line) is significantly broader than the instrumental profile (dotted line). The tertiary component can be well approximated as a convolution of the instrumental profile and a Gaussian with $\sigma = v \sin i$ of the third star. By deconvolving the tertiary peak in the broadening function with the instrumental profile, we recover 6.5 km s^{-1} as the projected rotational velocity of the 3rd star, a reasonable value for a G- or K-type dwarf (Nielsen et al. 2013).

3.2. Joint Bayesian Analysis of the Broadening Functions and Light Curves

The ability to measure $l3$ directly from the broadening function makes it possible to set it as a fixed parameter, empowering the BF and the LC to better constrain the other system parameters. For this reason, we both measure and remove tertiary components from BFs before feeding them into the joint-fitting pipeline. If the third light fraction is small ($l3 \lesssim 0.2$), we model it with a Gaussian function and subtract it from the overall BF. However, if the third light fraction is large ($l3 \gtrsim 0.2$), we model the tertiary using the BF of a narrow-lined single star. This second approach is required because a BF that includes a bright, narrow tertiary exhibits additional features (i.e., nonphysical artifacts from the single value decomposition) that may be comparable in strength to the signal from the inner binary. Figure 3 presents BFs of the triple system V1187 Her corresponding to two different orbital phases of the inner eclipsing binary, $\phi = 0.47$ (top two panels) and $\phi = 0.73$ (bottom two panels). The blue lines in the left two panels show the raw BFs of the target, which include both the large, narrow tertiary component at 0 km s^{-1} and the nonphysical artifacts associated with it. These artifacts can be reproduced and removed by subtracting a shifted and scaled BF of a slowly rotating single star (orange lines in the left two panels) using the same stellar template. The alignment of the artifacts in the two left panels indicates that the locations of these features are not fixed in velocity, but are fixed relative to the strongest component in the BFs. Each of the right two panels compares the results of subtracting a Gaussian fit (blue curves) versus subtracting the shifted, scaled single-star BF (orange curves). We find that the latter method is preferable, because it removes BF artifacts, thereby more clearly revealing the signature of the other BF components and eliminating potential false positives (e.g., the feature near 400 km s^{-1} in the upper-right panel). It also allows for more reliable velocity measurements of the binary components (e.g., eliminating the shift in the apparent location of the secondary in the bottom-right panel). Once the

tertiary's contribution to the system's radial velocity profile is characterized and removed, the system's BF can be used in tandem with its LC to more tightly constrain system parameters.

K22 used the PHOEBE (vers. 2.2; Prša 2018) code to model the Kepler LCs and retrieve posterior distributions of fundamental system parameters—five for contact systems and six for detached systems. However, degeneracies between parameters (e.g., third light and mass ratio) can produce highly uncertain and/or incorrect solutions. The addition of kinematically resolved spectral data near each of the two quadrature phases makes it possible to break these degeneracies. The two spectral BFs yield q and the relative sizes of the stars (R_2/R_1). When combined with an LC, which encodes information about orbital inclination, the BFs (which also contain information about inclination through the velocity width of the profile) permit measurements of the individual component masses and radii (under the reasonable assumption of spin–orbit synchronization). The BFs also reveal the physical geometry of the system, i.e., contact or detached,[6] allowing the correct physical model to be used. Furthermore, the relative areas of each BF component reflect the relative luminosities of the two stars (as long as the temperatures are similar, as in a contact binary), allowing the data to also constrain the ratio of component temperatures. Finally, the presence of light from a third body, if appreciable, reveals itself in the BF as a narrow spike of width comparable to the instrumental spectral resolution (i.e., 4–10 km s^{-1} for typical G–K main-sequence dwarf tertiaries). We measure the fractional area of this third component in the BF and assign it as a fixed parameter in the models. Taken together, the BF and LC data enable tight constraints on all of the key system parameters with minimal degeneracy.[7]

Following K22 we generated PHOEBE (vers. 2.4) model Kepler K_p-band light curves, applying either contact or detached geometries[8] with a surface mesh of 6000 triangles. These models make use of the stellar atmospheric models of Castelli & Kurucz (2003). The phased model light curve contains 100 phase bins and adopts the orbital period, the reference time of deepest eclipse (t_0), and the primary star temperature (T_1) as fixed parameters from Kirk et al. (2016).[9] We included irradiated and reflected energy effects according to Horvat et al. (2019), as implemented in PHOEBE 2.4, as this subtle effect becomes significant for systems having low-amplitude light curves ($\Delta K_p \lesssim 2\%$) when $T_1 \neq T_2$.

In parallel with the light-curve modeling, we also used PHOEBE to produce model line profiles (LPs) at orbital phases matched to those of the BF data over a velocity range of -500–500 km s^{-1} in 2 km s^{-1} intervals. These synthetic data sets are directly comparable to the BF data. We invert the PHOEBE LP data sets from absorption to emission to facilitate comparison to the BF, then scale them by an arbitrary normalization to best match the BF amplitudes. The PHOEBE LPs do not include the light from a third star.[10]

We coupled the forward PHOEBE models of the light curve and line profiles to an `emcee` (Foreman-Mackey et al. 2013) Markov Chain Monte Carlo (MCMC) ensemble sampler to determine the locus of best-fitting parameters and define the size and shape of the global minimum in parameter space. In both cases, we fixed the third-light fraction at the value determined from the BF. Contact models used five free parameters with flat priors between the limits $0.0 < \cos i < 1.0$, $0.03 < f < 0.99$,[11] $-1.4 < \log q < 1.4$, $0 < l3 < 0.99$, $0.95 < T_2/T_1 < 1.05$, and $0.1\,M_\odot < M_1 < 4\,M_\odot$. Detached models had six free parameters: $\cos i$, $\log q$, T_2/T_1, M_1, R_1, and R_2/R_1. The sampler employed either 10 or 12 walkers (i.e., twice the number of free parameters) with 5000 steps per walker. As in K22, we found it practical to implement two rounds of MCMC sampling—the first dispersing the walkers widely over parameter space to identify the locus of the best-fitting parameters within the highly multimodal χ^2 hypersurface, and the second placing walkers initially near the global minimum to rigorously define the distribution of posterior probabilities.

The merit function characterizing the fitness of each model within `emcee` is the logarithm of the probability density function for a given χ^2 value with ν degrees of freedom.[12] Each of the two BFs were fit separately with different normalizations but under the constraint of a common systemic velocity. The RMS of the BFs at velocities 400–500 km s^{-1} (i.e., velocities more extreme than any stellar velocity) were used as a measure of the uncertainty on each spectral channel in calculating the χ^2 for each BF. The log probability from each BF fit was added to the log probability for the light-curve fit to obtain a total log(probability) characterizing the fitness of each model. Typically the χ^2 for the two BFs were comparable to one another, so that they each carried similar weight in the fitting. However, owing to the extremely high signal-to-noise ratio of the Kepler photometric data (typically 10^4:1, versus 50:1 or worse for the BF data) we scaled the χ^2 values from the light-curve fits by an arbitrary factor to approximate those of the BF fits. This prevented either the BF or LC data sets from dominating the goodness-of-fit metric. We found that it was possible to achieve better fits to either the two broadening functions or the single light curve separately. However, when all three data sets contributed equally in the fitting process, there was a necessary level of tension between them, but there also emerged a unique, well-constrained range of physical parameters for each close binary system.

4. Results

4.1. Close Binaries

We find that 13 of the 18 systems are close binaries, and all but one (KIC07766185) are best fit by a detached model. In most cases, the two components in a system are clearly separated in velocity space (e.g., KIC06670812), and in the other cases, the best-fitting temperature ratio is far enough from

[6] Clear separation of the BF peaks in velocity space is typically achieved in detached systems.

[7] All of the nominal models produce symmetric light curves. K22 noted evidence for additional physical features in nearly all of the Kepler close binaries—e.g., starspots or accretion streams—that can create light-curve asymmetries. Although such features can be modeled, they entail several additional free parameters that we do not consider here.

[8] We do not explicitly model the semidetached case where only one star overflows its Roche lobe. We consider this to be an intermediate case bounded by the detached and contact cases.

[9] Throughout this work we adopt the dynamical definition that the primary star is the more-massive star. This definition is different than that adopted by K22, who used the observational definition that the primary star produces the deeper eclipse.

[10] As of PHOEBE 2.4.

[11] This fillout factor lower limit of 0.03 was adopted primarily to avoid numerical difficulties that occur when the Roche Lobes are only tenuously in contact at low f.

[12] scipy.stats.chi2.logpdf(χ^2, ν).

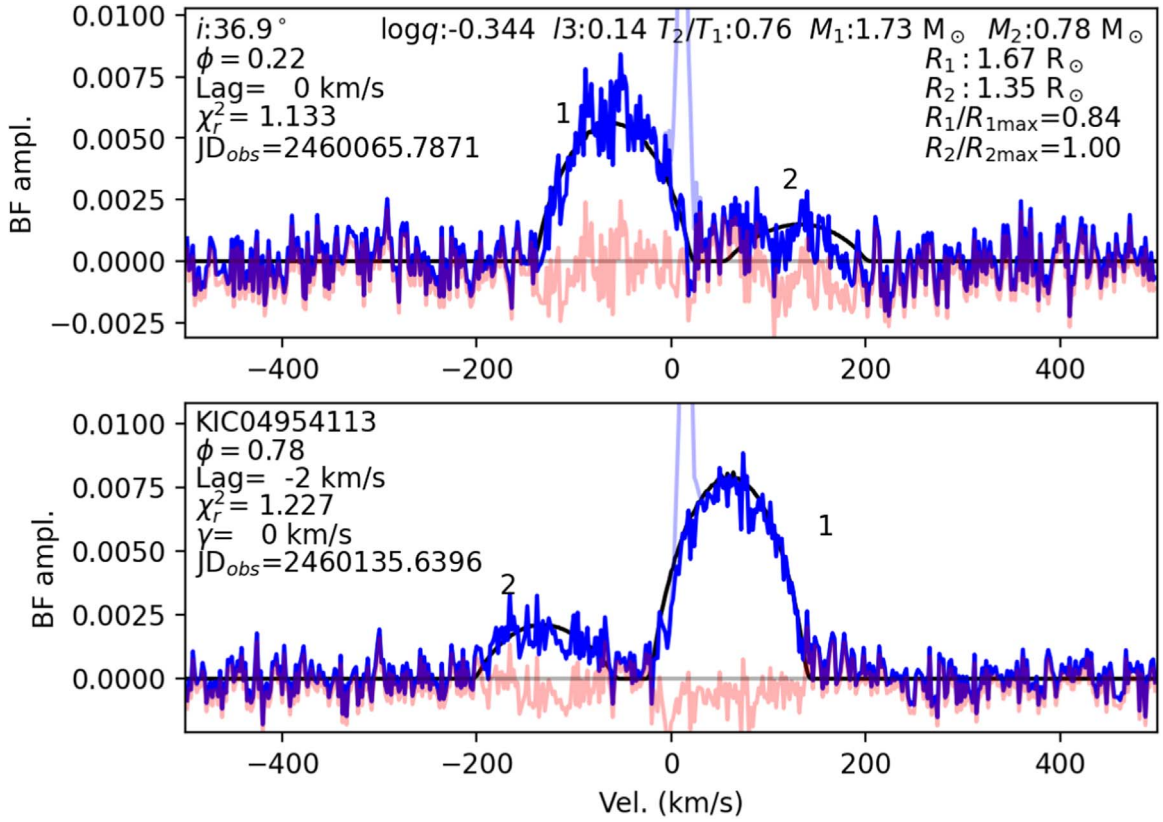

Figure 4. Broadening functions for KIC04954113 (blue lines) with joint PHOEBE fits (black lines) and residuals (salmon lines). The pale blue spike is the tertiary that we subtracted before performing the joint fit. Labels 1 and 2 denote the primary and secondary components. The text inside the panels gives the best-fitting parameters, distinct from the 50th percentile parameters given in the body of the paper and tables.

unity (i.e., $T_2/T_1 < 0.9$) to rule out a contact configuration (e.g., KIC04954113 and KIC07977261). In both K22 and the current work, we perform the Bayesian fitting over $\cos i$ and $\log q$ and present these values in the tables for each target. However, we translate these values into i and q in the text. Given that all contact and near-contact binary stars have components that depart from spherical geometry, all of the radii discussed below are volume-equivalent radii (i.e., the radius of a sphere of equivalent volume).

4.1.1. KIC04954113

KIC04954113 is a close binary system with an orbital period of $P = 0.668$ day (Kirk et al. 2016) and an effective temperature of $T_{\rm eff} = 7730$ K (Zhang et al. 2019). Its Kepler LC exhibits significant variability and unequal primary and secondary minimum depths of 0.0331 and 0.0246. K22 explained these shallow minima with a low inclination of $i = 18.^{\circ}2^{+1.^{\circ}2}_{-0.^{\circ}9}$ while keeping the mass ratio moderate ($q = 0.66^{+0.09}_{-0.10}$) and the third light contribution low ($l3 = 0.09^{+0.09}_{-0.05}$).

Figure 4 displays the quadrature BFs and best-fitting model line profile of KIC04954113. The black curves show the best detached joint BF–LC models with optimal velocity shifts (given by the Lag parameter in each panel), and the salmon lines show the residuals. The pale blue spike near zero radial velocity is the contribution from the tertiary that we fit with a Gaussian then subtracted before performing the joint fit. From fitting the tertiary, we find a third light fraction of $l3 = 0.14$, which we hold fixed when modeling the system. Figure 5 shows the LC for KIC04954113, and the magenta curve shows the best joint fit. Text within each figure gives the best-fitting parameters for the system. Table 3 lists the 16th, 50th, and 84th percentile values for each free parameter.

While the BF in Figure 4 does not immediately reveal the geometry of KIC04954113, the temperature ratio required by the vastly different amplitudes in the BF, $T_2/T_1 = 0.773^{+0.016}_{-0.014}$, indicates that it cannot be contact. Note that this is the most probable temperature ratio (50th percentile), and is slightly different than the best-fitting temperature ratio displayed in Figures 4 and 5. In contrast to the best fit to the LC found by K22, we find that the inclination is $i = 37^{\circ}{}^{+3^{\circ}}_{-2^{\circ}}$ and the mass ratio is $q = 0.46^{+0.02}_{-0.02}$. The radius ratio ($R_2/R_1 = 0.81^{+0.02}_{-0.03}$) is much higher than one would expect from the moderate mass ratio. In fact, our model shows the secondary completely filling its inner Roche surface ($R_2/R_{2\,\rm max} = 1.00$) while the primary does not ($R_1/R_{1\,\rm max} = 0.84$),[13] making KIC04954113 a semi-detached system. The BF in the top panel of Figure 4 features a sizeable dip in the center of the secondary component, suggesting the presence of large starspots on the secondary star. This would explain the variability in the LC seen in Figure 5, provided the starspots are variable in size and/or location. It is also consistent with the eclipse timing variations (ETVs) seen in the system,[14] where the timing variations of the primary and secondary eclipses mirror each other. ETVs that show such anticorrelated changes in the timing of the primary and secondary minima are an indicator of spots on a close

[13] $R_{\rm max}$ is the radius of a sphere of equivalent volume to a star that fills its inner Roche lobe (i.e., reaches the L1 point).

[14] Plots at http://keplerebs.villanova.edu/plots/?k=4954113.00&cadence=lc&kind=etv.

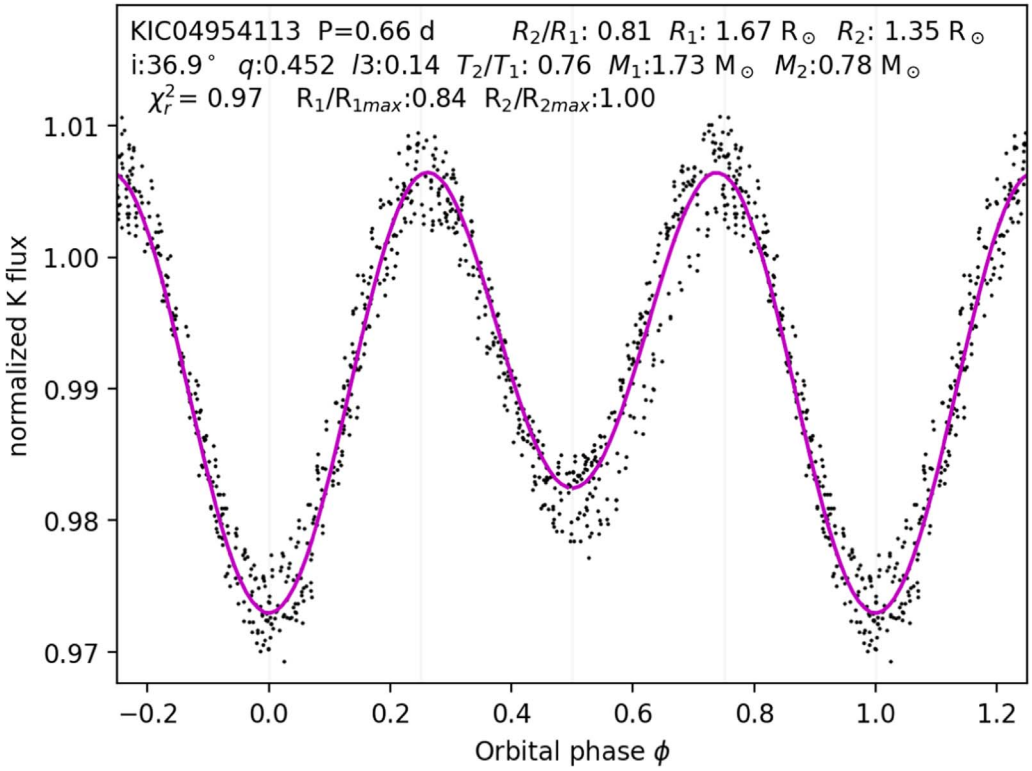

Figure 5. Phase-folded Kepler data for KIC04954113 with the joint fit LC solution (magenta curves).

Table 3
Bayesian 16th, 50th, and 84th Percentile Values for the System Parameters for KIC04954113

	16th	50th	84th
$\cos i$	0.765	0.795	0.818
$\log q$	−0.354	−0.334	−0.313
T_2/T_1	0.759	0.773	0.789
M_1	1.437	1.685	1.920
R_1	1.541	1.650	1.751
R_2/R_1	0.778	0.807	0.826

binary (Tran et al. 2013). A second explanation proposed for the LC variability is that—in addition to the system being an ellipsoidal variable—the primary star exhibits δ Scuti oscillations (Gaulme & Guzik 2019).

Figure 6 shows the posterior probability distributions for the system parameters for KIC04954113. They are all unimodal and most are roughly Gaussian. The individual panels reveal correlations between the posterior probability distributions of pairs of parameters. For example, the middle-left panel showcases the steep dependence of M_1 on $\cos i$. This reflects the fact that the retrieved primary mass depends on the orbital inclination as $M_1 \propto (\sin i)^{-3}$. For example, a change from $i = 15°$ to $i = 19°$ entails a factor of 2 change in mass. The posterior probability distribution for R_1 also depends on $\sin i$, though much less sensitively. This is to be expected given that $R_1 \propto (\sin i)^{-1}$. The implication of these degeneracies is that systems with poorly constrained inclinations (e.g., due to starspots or third light changing the shape and/or depth of the LC) can yield inaccurate values for system parameters, especially the component masses.

4.1.2. KIC05802834

KIC05802834 is a close binary with a period of 1.09 days and an effective temperature likely between 6077 K (Prša et al. 2011) and 6699 K (Zhang et al. 2019). The Kepler LC exhibits shallow, uneven primary and secondary minima (0.040 and 0.027). The variability in the amplitude of the LC suggests the presence of starspots. This is substantiated by the large anticorrelated ETVs of the primary and secondary minima of over 30 minutes (Balaji et al. 2015). The K22 contact fit for KIC05802834 finds a moderate mass ratio of $q = 0.49^{+0.12}_{-0.09}$, a large fillout factor of $f = 0.76^{+0.16}_{-0.21}$, a low inclination of $i = 20.^{\circ}6^{+2.^{\circ}0}_{-1.^{\circ}5}$, and a small third light contribution of $l3 = 0.12^{+0.13}_{-0.08}$.

Figure 7 shows the BFs for KIC05802834. The light gray curves show the best detached joint BF–LC models at zero systemic velocity.[15] The BFs (both taken near $\phi = 0.25$) show that there is no detectable third component in the system. And while they feature a prominent, broad primary, they also show that there is no detectable second component in the system. However, the anticorrelated ETVs from the Kepler photometry argue strongly that KIC05802834 is a binary star. Therefore, the two components must have a luminosity ratio so extreme that the secondary does not make an appearance in the BF. In order to achieve such an extreme luminosity ratio, the two stars must have very different temperatures, effectively ruling out a contact configuration.

Figure 8 shows the system's Kepler LC. Given the low luminosity of the secondary, most of the modulation in the LC is likely the result of the nonspherical nature of the primary. Table 4 compiles the 16th/50th/84th percentile values for key system parameters. We find a temperature ratio for this system

[15] They were not visible in Figure 4 due to the small system velocity.

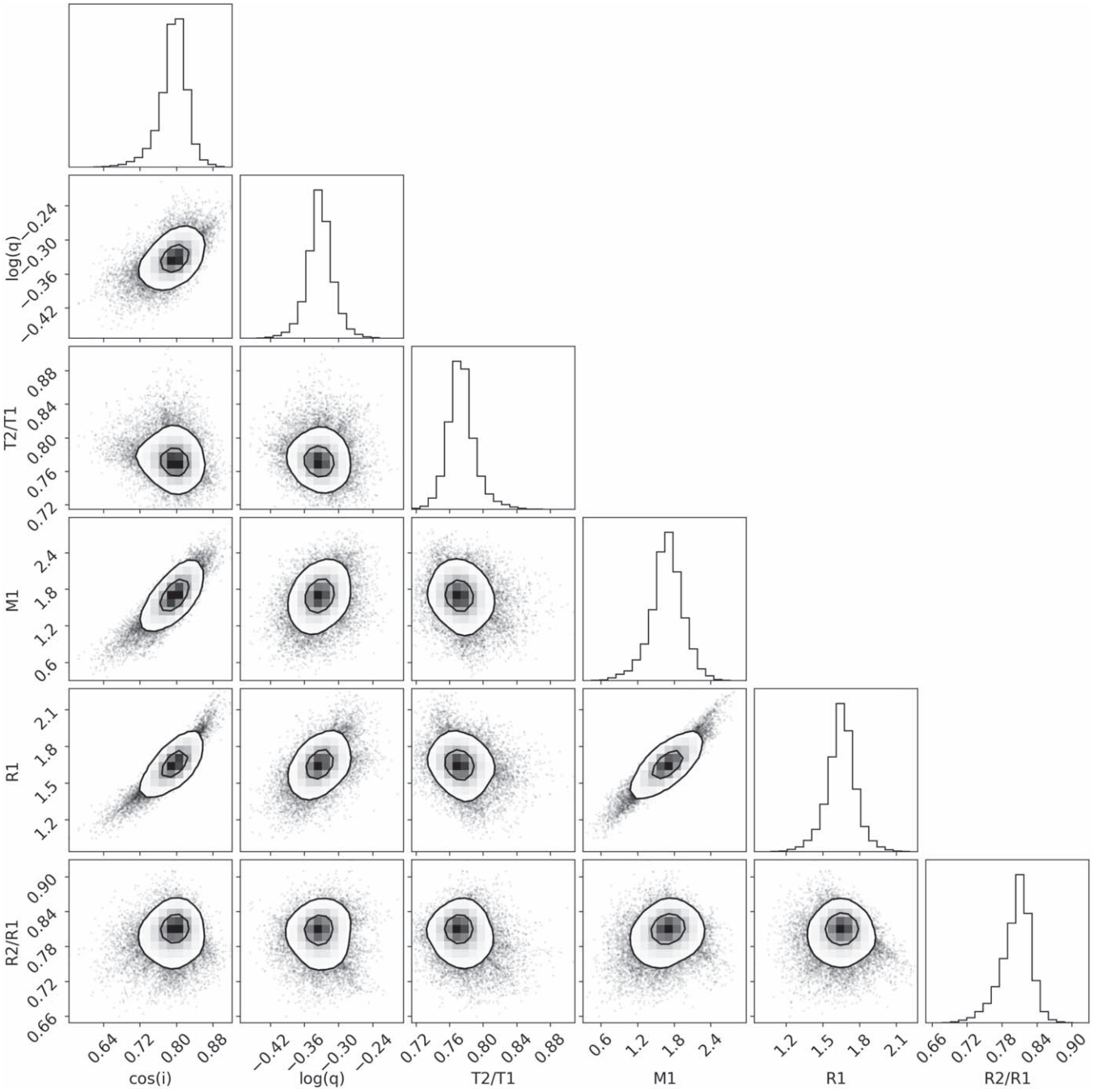

Figure 6. Posterior probability distributions on system parameters for KIC04954113 from the MCMC Bayesian analysis.

of $T_2/T_1 = 0.717^{+0.004}_{-0.002}$. This is an upper limit given that the fitting routine was constrained to temperature ratios greater than 0.7. Again, this temperature ratio reveals the detached nature of the system. The mass ratio is $q = 0.266^{+0.020}_{-0.013}$, somewhat smaller than the K22 result. The radius ratio we obtain is $R_2/R_1 = 0.594^{+0.013}_{-0.010}$, which should be taken with caution, given that the secondary does not make an appearance in the BF. However, because of reflection effects and the very unequal temperatures of the binary components, the LC is sensitive to the size of the secondary. Irradiation effects are required to fit the unequal minima in the LC. In contrast to the contact model of K22, we find an inclination of $i = 47.^{\circ}9^{+0.^{\circ}7}_{-0.^{\circ}8}$. We obtain a system velocity of -52 km s^{-1}, in agreement with the Gaia radial velocity for this system of -50 ± 8 km s^{-1}. The primary mass and radius are $M_1 = 1.84^{+0.13}_{-0.10}\,M_\odot$ and $R_1 = 2.51^{+0.05}_{-0.05}\,R_\odot$. Based on these results and the Zhang et al. (2019) effective temperature of 6699 K, we conclude that the system consists of an early F-type primary and an early M-type secondary, both with radii larger than main-sequence values.

4.1.3. KIC06670812

KIC06670812 (HD 176229) is by far the brightest target in our sample with a Kepler magnitude of $K_p = 7.24$. Unsurprisingly, it is also the closest at a distance of only 118 pc. Its relatively long period of 1.74 days suggests a detached geometry, but its smooth light curve is indicative of either a

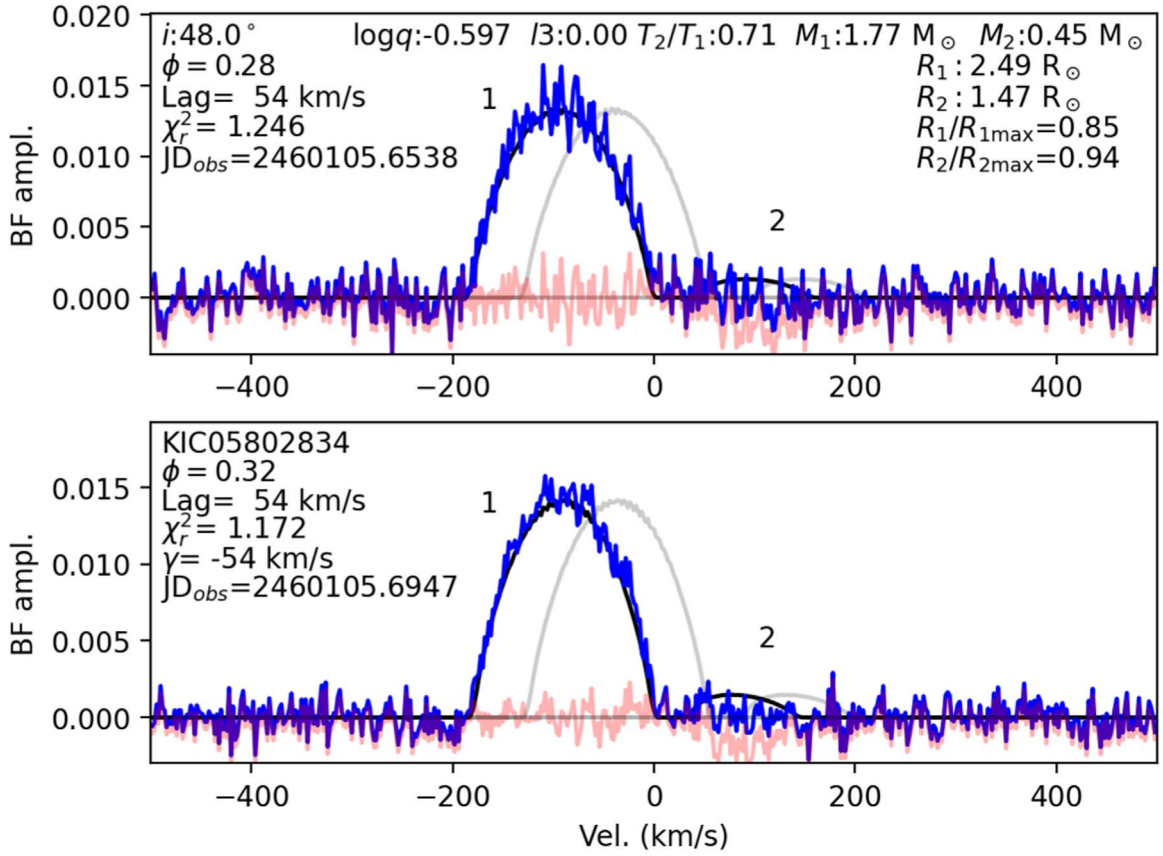

Figure 7. Broadening functions for KIC05802834, as in Figure 4. Both BFs correspond to exposures taken near the first quadrature (i.e., near $\phi = 0.25$).

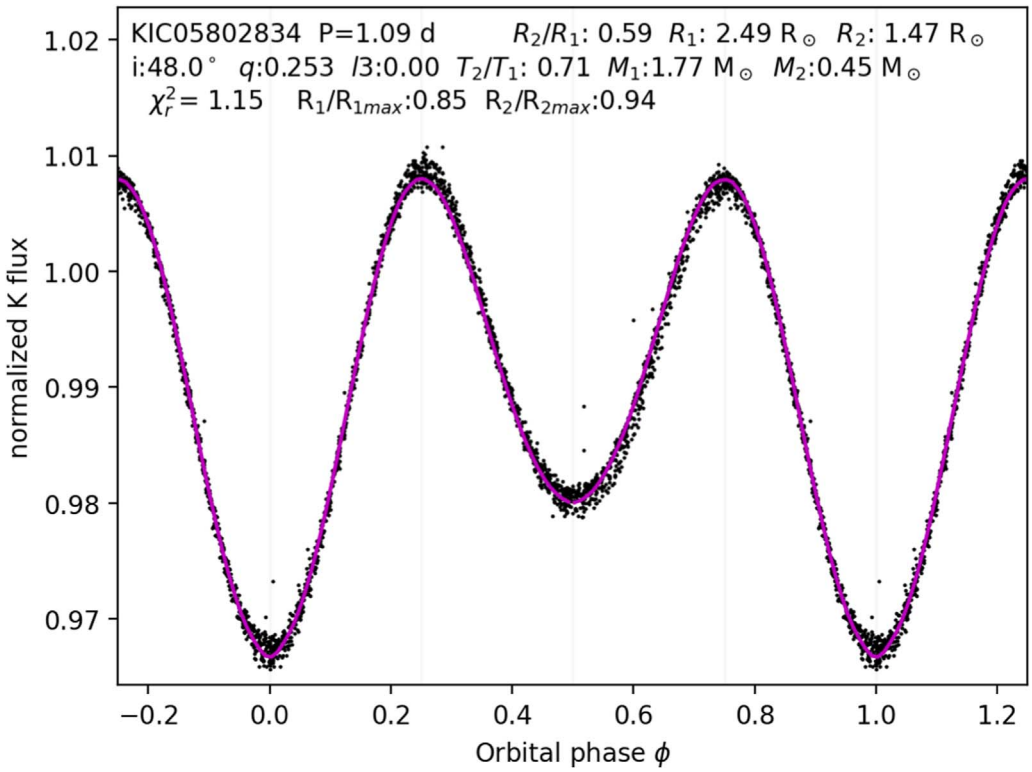

Figure 8. Phase-folded Kepler data for KIC05802834 with the joint fit LC solution (magenta curves), as in Figure 5.

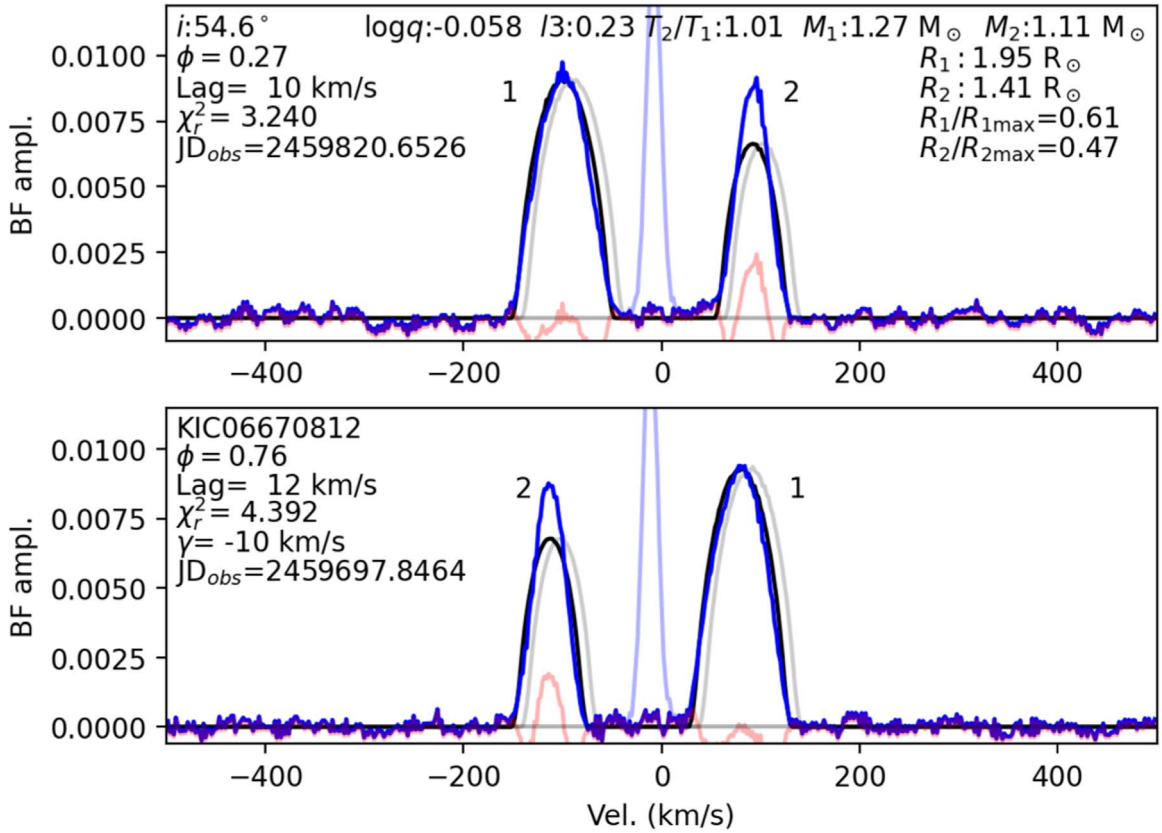

Figure 9. Broadening functions for KIC06670812, as in Figure 4.

Table 4
Bayesian 16th, 50th, and 84th Percentile Values for the System Parameters for KIC05802834

	16th	50th	84th
$\cos i$	0.661	0.671	0.681
$\log q$	−0.597	−0.575	−0.543
T_2/T_1	0.715	0.717	0.721
M_1	1.739	1.843	1.972
R_1	2.457	2.507	2.557
R_2/R_1	0.583	0.594	0.607

contact binary or a detached ellipsoidal variable. Previous studies have classified KIC06670812 anywhere between F0V (Cannon & Pickering 1993) and F6V (Nordström et al. 2004). The Kepler LC is remarkably free of dispersion and variability for being so low amplitude (1% eclipse depths). Along with the above range of spectral types, this points to an absence of starspots and pulsation in either of the components of KIC06670812. To fit the low amplitude of the LC, the contact model of K22 settled on a large third light fraction of $l3 = 0.883^{+0.017}_{-0.015}$ and a low orbital inclination of $i = 39^{\circ}{}^{+3\circ}_{-3\circ}$. They found a moderate mass ratio of $q = 0.56^{+0.07}_{-0.07}$.

Figure 9 displays the quadrature BFs of KIC06670812 and the best-fitting joint model, as in Figure 4. The broadening function clearly shows that KIC06670812 is a detached system. Figure 10 shows the Kepler LC for KIC06670812 along with the best joint fit, where we have fixed the third light fraction at $l3 = 0.23$. Table 5 compiles the 16th/50th/84th percentile values for key system parameters. From the joint fit, we find that the mass ratio is $q = 0.8754^{+0.0012}_{-0.0008}$, revealing similar masses for the two components. This is much larger and more precise than the value found by K22 based on the light curve alone and a contact binary model. The orbital inclination of the system is moderate and well-constrained at $i = 54.^{\circ}63^{+0.^{\circ}18}_{-0.^{\circ}11}$. The Heliocentric systemic velocity is $v_0 = -10\,\mathrm{km\,s^{-1}}$.

We find a 50th percentile mass for the primary and the secondary of $M_1 = 1.2740^{+0.0014}_{-0.0015}\,M_\odot$ and $M_2 = 1.1153 \pm 0.0018\,M_\odot$. These masses correspond to main-sequence radii of $1.58\,R_\odot$ and $1.36\,R_\odot$ (Pecaut & Mamajek 2013), yielding an expected radius ratio $R_2/R_1 = 0.86$. However, we find a radius ratio of $R_2/R_1 = 0.721^{+0.003}_{-0.002}$, a primary stellar radius of $R_1 = 1.952^{+0.004}_{-0.002}\,R_\odot$, and a secondary radius of $R_2 = 1.408 \pm 0.005\,R_\odot$. These large radii are reflected in the ratios $R_1/R_{1\,\mathrm{max}} = 0.61$ and $R_2/R_{2\,\mathrm{max}} = 0.47$, which also reveal that the primary component fills more of its Roche lobe than secondary. For these masses, we would expect primary and secondary temperatures of 6750 and 6350 K, respectively, yielding a predicted $T_2/T_1 = 0.94$. However, we find a temperature ratio very close to unity, $T_2/T_1 = 1.006^{+0.002}_{-0.002}$ (similar to the $T_2/T_1 = 0.98$ inferred by K22). This is likely due to radiative heating of the secondary by the primary, given that the surfaces of the two are separated by only $1.7\,R_\odot$. This temperature ratio near unity is further supported by our experiments running the BF code using stellar templates ranging from 4000–8000 K; the ratio of BF areas only changes by ∼5% across this wide temperature range.

In the context of a contact model, the low amplitude of the LC (∼1%) requires either a low inclination and/or a large third light fraction. The contact model for KIC06670812 from K22 opted for a mixture of both, settling on $i = 36.7$ and $l3 = 0.868$. The BF demonstrates that the low amplitude of the minima is a consequence of the detached geometry of the system;

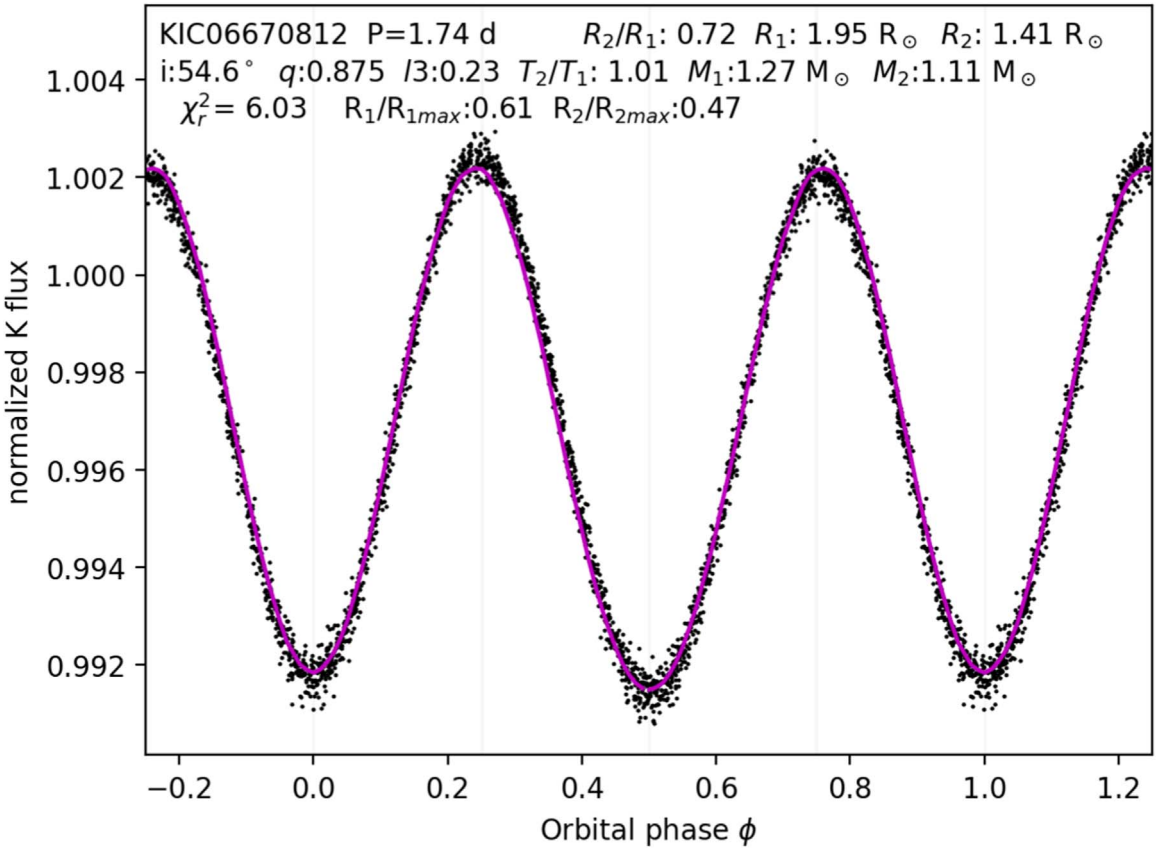

Figure 10. Phase-folded Kepler data for KIC06670812 with the joint fit LC solution (magenta curves), as in Figure 5.

Table 5
Bayesian 16th, 50th, and 84th Percentile Values for the System Parameters for KIC06670812

	16th	50th	84th
$\cos i$	0.576	0.579	0.580
$\log q$	−0.058	−0.058	−0.057
T_2/T_1	1.005	1.006	1.009
M_1	1.272	1.274	1.275
R_1	1.950	1.952	1.956
R_2/R_1	0.719	0.721	0.724

KIC06670812 is an ellipsoidal variable, likely in a tertiary system. The third light fraction is in the range 21%–23%. The tertiary has radial velocity $v_{\rm rad} \approx -10\,{\rm km\,s^{-1}}$. From the third light fraction and the masses of the primary and secondary, we estimate that the tertiary has a luminosity of $L_3 \approx 2.1\,L_\odot$, corresponding to an F7V or F8V star, consistent with our value for the projected rotation rate $v_{\rm R} \sin i \approx 11\,{\rm km\,s^{-1}}$ (Nielsen et al. 2013).

4.1.4. KIC06692340

KIC06692340 ($T_{\rm eff} = 6135$ K) boasts one of the most complex light curves in our sample. It features time-variability, unequal primary and secondary minima (0.0145 and 0.0178), uneven maxima (i.e., the O'Connell effect), and ETVs well in excess of 20 minutes. The shifts in the timing of the primary minimum and the secondary minimum mirror each other, suggesting that KIC06692340 hosts starspots. Unsurprisingly, the LC led K22 to arrive at a poorly constrained mass ratio of $q = 0.7^{+0.3}_{-0.2}$, an inclination of $i = 19^{\circ}{}^{+7\circ}_{-4\circ}$, and a third light contribution of $l3 = 0.6^{+0.2}_{-0.3}$.

The BF of KIC06692340 in Figure 11 is much less feral than its LC (Figure 12), and immediately reveals the absence of a third light, in contrast to the K22 solution. Table 6 compiles the 16th/50th/84th percentile values for key system parameters. Most importantly, a satisfactory fit to both the LC and the BFs requires substantially different surface temperatures for the two components ($T_2/T_1 = 0.868^{+0.012}_{-0.013}$), suggesting a detached or semidetached configuration. We find a mass ratio for the system of $q = 0.610^{+0.021}_{-0.018}$ and an inclination of $i = 17.^{\circ}3^{+2.^{\circ}5}_{-1.^{\circ}6}$, both in agreement with the K22 contact solution. However, the relatively small uncertainty on orbital inclination translates to large uncertainties on component masses, $M_1 = 1.3^{+0.4}_{-0.4}\,M_\odot$ and $M_2 = 0.8 \pm 0.3\,M_\odot$. The primary radius is $R_1 = 1.69^{+0.15}_{-0.22}$ $R_\odot$ and the radius ratio is $R_2/R_1 = 1.3^{+1.0}_{-0.4}$. Both components are almost completely filling their Roche lobes, with $R_1/R_{1\,\rm max} = 0.95$ and $R_2/R_{2\,\rm max} = 1.00$. This is likely why K22 found values for q and i very similar to that of the present work using a contact model, despite their incorrect—but poorly constrained—value for l_3.

4.1.5. KIC07766185

KIC07766185 is a binary system with an orbital period of 0.835 days. Reports of its effective temperature range from of 5977 K (Prša et al. 2011) to over 6600 K (Frasca et al. 2016; Zhang et al. 2019). Its Kepler LC is very clean and shows almost no ETVs. It has deep, slightly unequal primary and secondary minima depths of 0.40 and 0.36. It was this large amplitude of modulation that led K22 to find a large mass ratio of $q = 0.9^{+0.2}_{-0.2}$, a small third light fraction of $l3 = 0.08^{+0.04}_{-0.03}$, and an inclination of $i = 74.^{\circ}9^{+1.^{\circ}0}_{-0.^{\circ}9}$. Additionally, they found

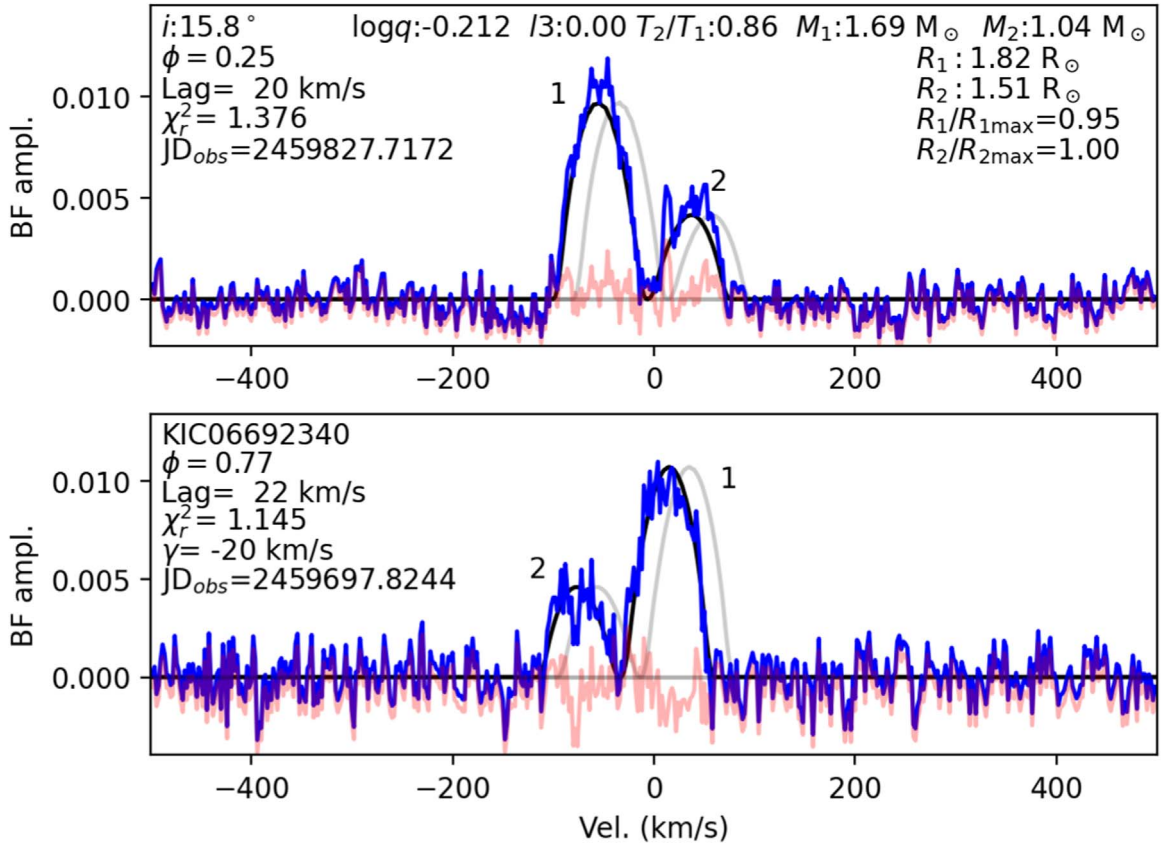

Figure 11. Broadening functions for KIC06692340, as in Figure 4.

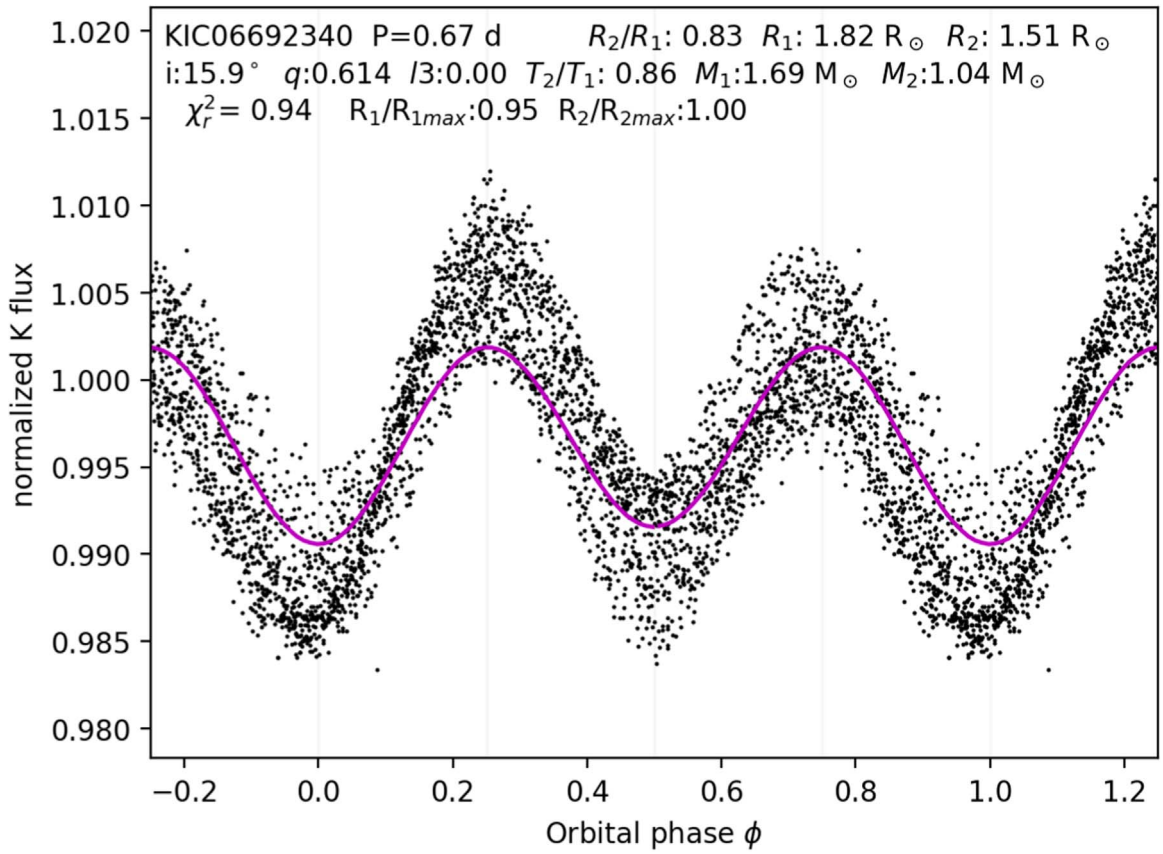

Figure 12. Phase-folded Kepler data for KIC06692340 with the joint fit LC solution (magenta curves), as in Figure 5.

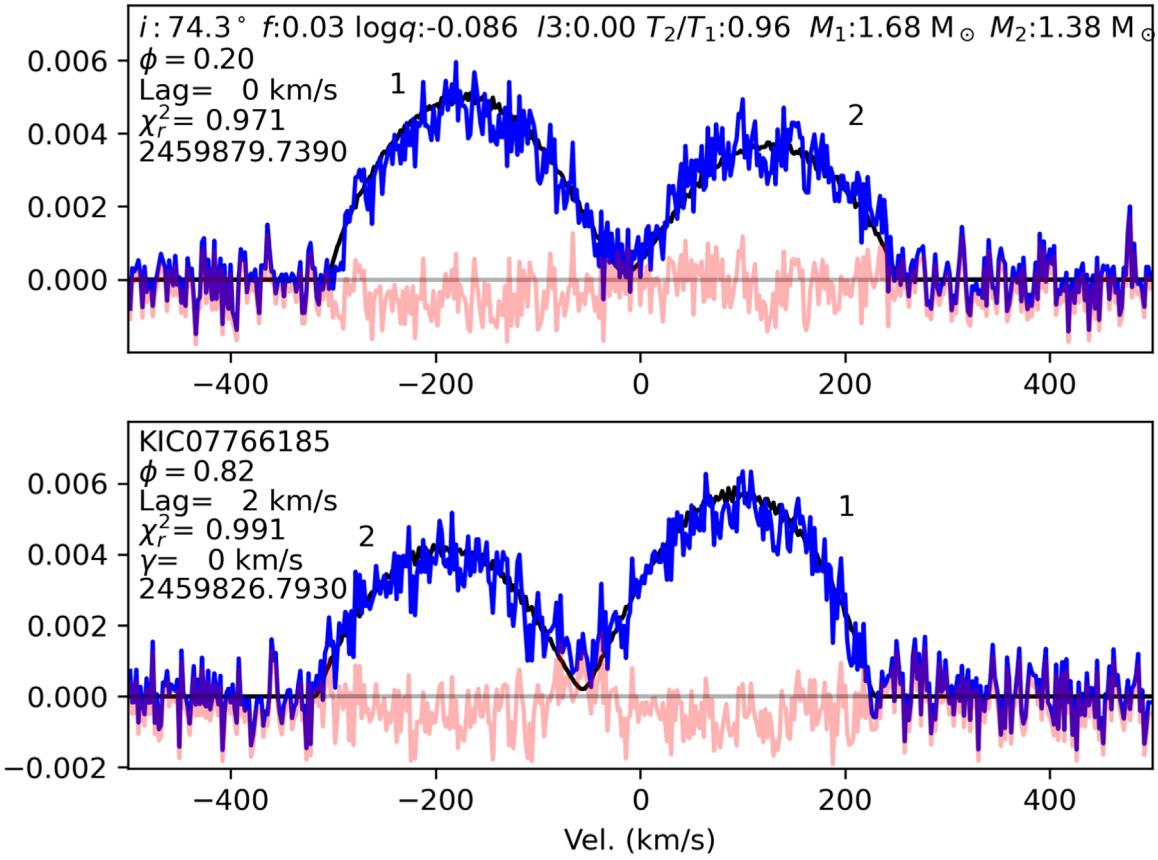

Figure 13. Broadening functions for KIC07766185, as in Figure 4.

Table 6
Bayesian 16th, 50th, and 84th Percentile Values for the System Parameters for KIC06692340

	16th	50th	84th
$\cos i$	0.941	0.955	0.963
$\log q$	−0.228	−0.215	−0.200
T_2/T_1	0.855	0.868	0.880
M_1	0.892	1.335	1.730
R_1	1.469	1.694	1.847
R_2/R_1	0.906	1.305	2.333

the temperature ratio to be $T_2/T_1 = 0.960^{+0.004}_{-0.003}$ and the fillout factor to be $f = 0.06^{+0.02}_{-0.02}$. Given the low fillout factor, detached models can fit the system equally well, leading them to assign the system an ambiguous geometry. Ding et al. (2021) also implemented an MCMC approach to model Kepler LCs, and included KIC07766185 in their sample. They obtained $q = 0.90$, $i = 73.^{\circ}45$, and $T_2/T_1 = 0.96$, in remarkable agreement with K22.

The system's BF (Figure 13) bears out the low fillout factor found by K22, showing that the bridge between the two components dips almost down to 0. This low fillout factor is also reflected in the shoulders of the system's LC in Figure 14. The BF also reveals that the mass ratio is large, as the two components' radial velocities change by similar amounts from one quadrature to the next. Table 7 compiles the 16th/50th/84th percentile values for key system parameters for the contact model fit. Indeed, our joint fit finds that $f = 0.08^{+0.03}_{-0.03}$ and $q = 0.80^{+0.05}_{-0.04}$. The third light fraction is $l3 = 0.00$, the temperature ratio is $T_2/T_1 = 0.969^{+0.018}_{-0.019}$, and the orbital inclination is $i = 72.^{\circ}4^{+1.^{\circ}1}_{-0.^{\circ}7}$, all of which are in excellent agreement with the K22 contact solution. We find primary and secondary masses of $M_1 = 1.76^{+0.13}_{-0.14}\,M_{\odot}$ (corresponding to a main-sequence late-A star) and $M_2 = 1.41 \pm 0.13\,M_{\odot}$. These large masses suggest fully radiative stars, which may explain the absence of starspot effects in the LC. Attempts to perform a joint fit using a detached model result in both components filling their Roche lobes (i.e., $R_1/R_{1\,\max} = R_2/R_{2\,\max} = 1.00$). Detached solutions also fail to satisfactorily reproduce the LC. The literature universally agrees that $\log g > 4.0$ (Prša et al. 2011; Frasca et al. 2016; Zhang et al. 2019). Therefore, we conclude that KIC07766185 is a contact binary with a late A- or early F-type MS primary.

4.1.6. KIC07884842

Thanks to its relatively low apparent magnitude of $K_p = 9.60$ mag, the literature on KIC07884842 (HD 181491) goes back to the mid-twentieth century (Macrae 1952). Since then, reports of the system's spectral type have ranged from A2V (Frasca et al. 2016) to B9V (Ramírez-Preciado et al. 2020). Together with its Gaia parallax distance of only 537 pc, this makes it the second brightest target in our sample. The Kepler LC shows very unequal primary and secondary minima (0.014 and 0.007) as well as asymmetries on either side of these minima. Curiously, this early-type binary also features additional aperiodic variability at the ∼0.1% level, suggesting the presence of starspots (Balona 2017). The system's ETVs exhibit a fascinating trend over the 4 yr of Kepler photometry: the primary eclipses occur slowly but steadily later. For the first 2 yr, there appeared to be no change in the timing of the

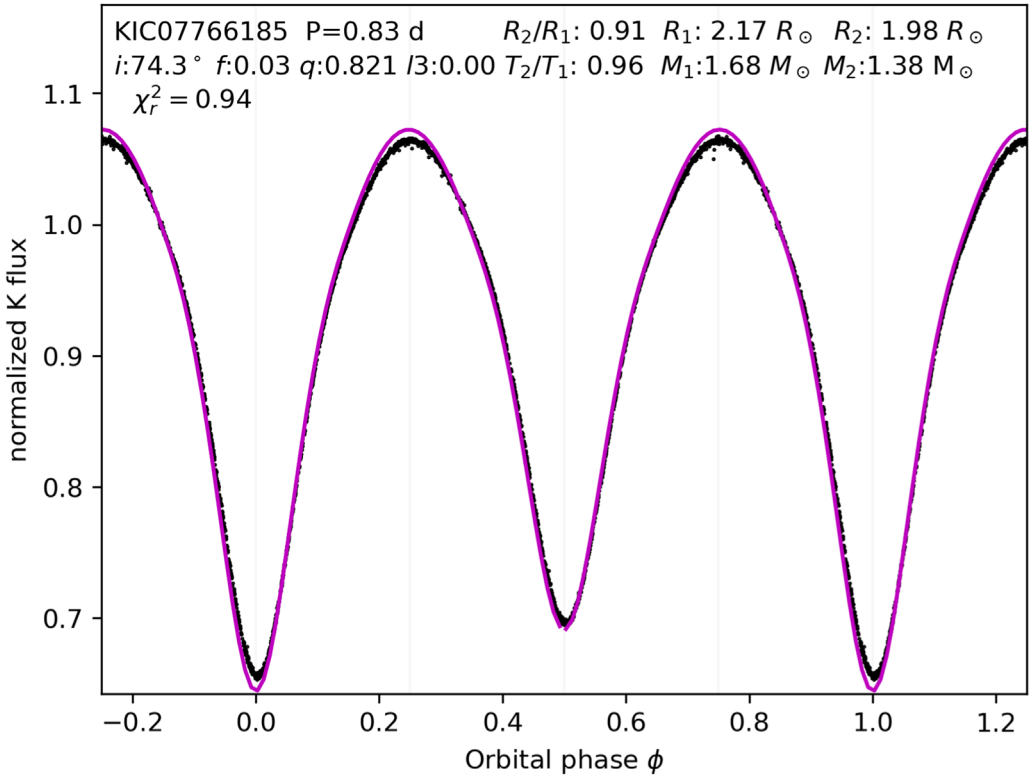

Figure 14. Phase-folded Kepler data for KIC07766185 with the joint fit LC solution (magenta curves), as in Figure 5.

Table 7
Bayesian 16th, 50th, and 84th Percentile Values for the System Parameters for KIC07766185

	16th	50th	84th
$\cos i$	0.285	0.303	0.315
f	0.047	0.077	0.103
$\log q$	−0.120	−0.096	−0.068
T_2/T_1	0.950	0.969	0.987
M_1	1.619	1.761	1.891

secondary eclipses, but during the last 2 yr, the secondary eclipses began occurring steadily earlier. This suggests the presence of a slowly migrating spot region that also changes in size. The contact model of K22 found an inclination of $i = 15^{\circ}{}^{+3}_{-3}{}^{\circ}_{\circ}$, a third light fraction of $l3 = 0.35^{+0.18}_{-0.23}$, and a mass ratio of $q = 0.31^{+0.17}_{-0.10}$. The large dispersions in these posterior parameters are largely a consequence of the shallow minima and the LC asymmetry and likely led to their classification of the system as ambiguous.

The BFs of KIC07884842 (Figure 15) clearly reveal both the detached nature of the system and the absence of a third stellar component (i.e., $l3 = 0.00$). It shows that the two components nearly trade places from one quadrature to the next, implying a large mass ratio. The similar heights and widths of the components indicate that the temperature and radius ratios are also near unity. Combining the information in the BFs with the LC in Figure 16 yields values for these three ratios of $q = 0.7301^{+0.0005}_{-0.0018}$, $T_2/T_1 = 0.906^{+0.006}_{-0.002}$, and $R_2/R_1 = 0.984^{+0.015}_{-0.058}$. The joint fit gives an inclination of $i = 46.^{\circ}3^{+0.^{\circ}4}_{-0.^{\circ}3}$, which leads to our determinations of primary mass and radius of $M_1 = 2.21^{+0.02}_{-0.08}\,M_\odot$ and $R_1 = 1.712^{+0.051}_{-0.012}\,R_\odot$. The discrepancy between the lag parameters in the two panels of Figure 15 results from a known wavelength calibration problem on the night when the $\phi = 0.77$ exposure was obtained. Of greater consequence is the poor match between our nominal spot-free model and the LC of the system. The model fails to fully reproduce either the asymmetry of the LC or the difference in depths of its minima, meaning that the uncertainty on the retrieved inclination is certainly larger than the formal errors compiled in Table 8. A system like KIC07884842 with both LC asymmetries and unequal minima is very difficult to characterize, even with the combined power of the system's BF and LC. Nevertheless, the primary mass we retrieve is in reasonable agreement with a B9–A2 dwarf.

4.1.7. KIC07976783

KIC07976783 is a close binary with a period of $P = 1.209$ days, a spectral type of A6V (Frasca et al. 2016), and an effective temperature of 7937 K (Prša et al. 2011). Its LC features shallow minima (0.57%) and ETVs in excess of 10 minutes. A number of papers identified this system as both a close binary and a pulsating variable (Balona 2018; Barceló Forteza et al. 2018; Gaulme & Guzik 2019), claiming that it exhibits both δ Scuti and γ Doradus activity. K22 listed this system as having a mass ratio of $q = 0.91^{+0.22}_{-0.16}$. To attain the shallow minima shown in the LC in spite of this high mass ratio, their model for this system settled on a low inclination of $i = 12.^{\circ}8^{+2.^{\circ}8}_{-2.^{\circ}6}$ and a high third light fraction of $l3 = 0.61^{+0.13}_{-0.21}$.

The BF (Figure 17) unambiguously reveals that KIC07976783 is a detached binary. Figure 18 shows the joint fit to the LC, and Table 9 compiles the 16th/50th/84th percentile values for key system parameters. We obtain a mass ratio for the system of $q = 0.603^{+0.006}_{-0.007}$. In contrast to the solution of K22, we find no third light in the system. The fit yields a moderate inclination of $i = 43.^{\circ}1^{+0.^{\circ}4}_{-0.^{\circ}3}$, which yields a

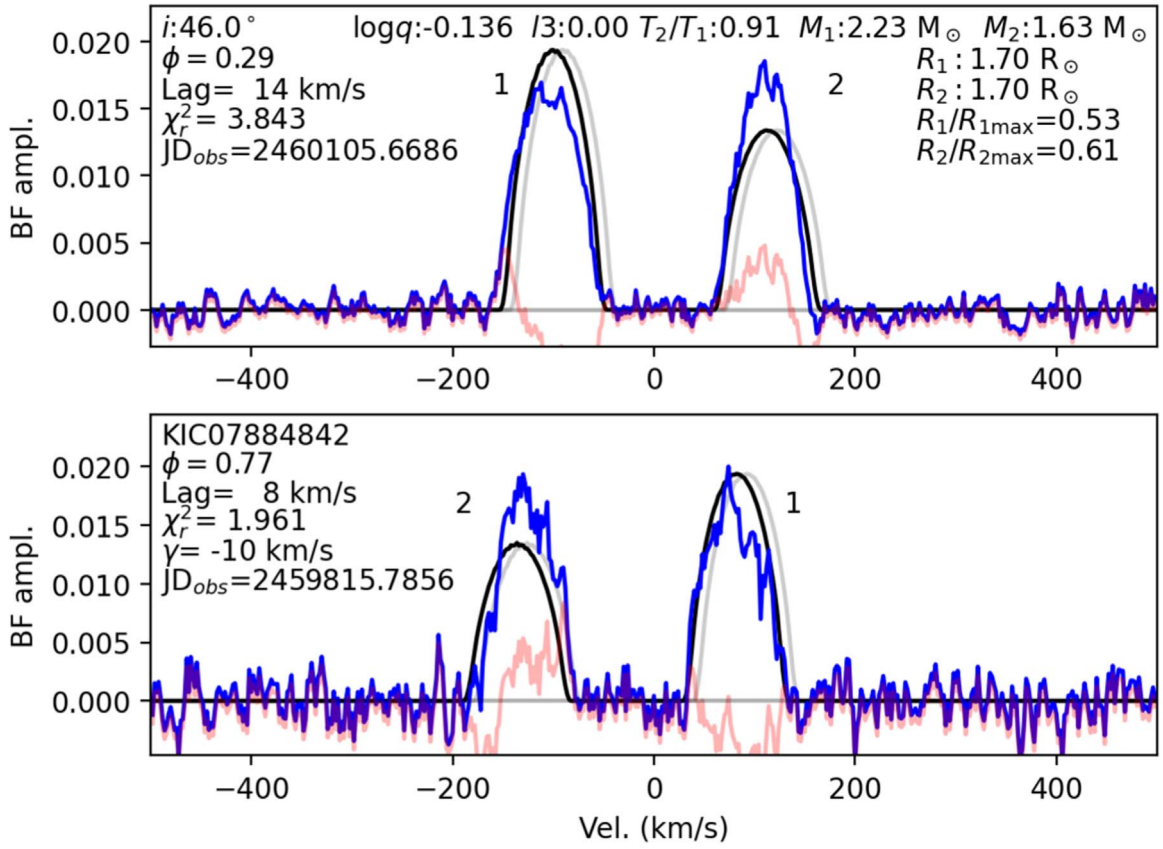

Figure 15. Broadening functions for KIC07884842, as in Figure 4.

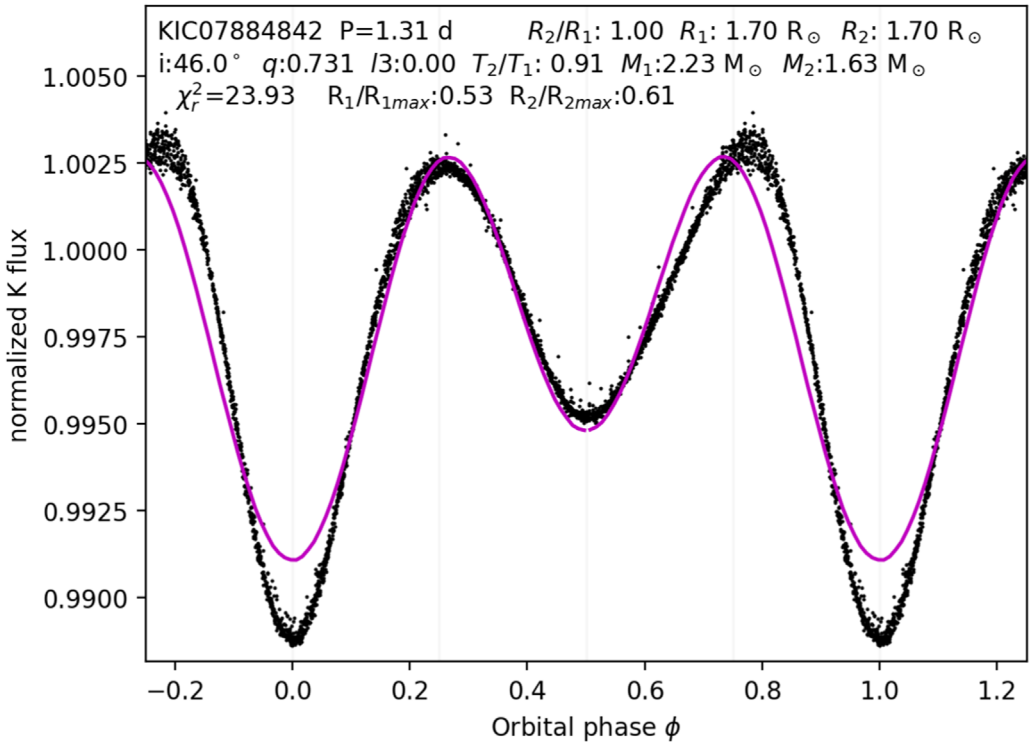

Figure 16. Phase-folded Kepler data for KIC06670812 with the joint fit LC solution (magenta curves), as in Figure 5.

primary mass and radius of $M_1 = 1.995^{+0.004}_{-0.007}\,M_\odot$ and $R_1 = 1.658^{+0.009}_{-0.010}\,R_\odot$. It seems possible that the combination of ellipsoidal variations and pulsational variations may compromise the light-curve fit to a degree that precludes an accurate retrieval of the inclination, adversely affecting the estimates of component masses, in particular. We find a

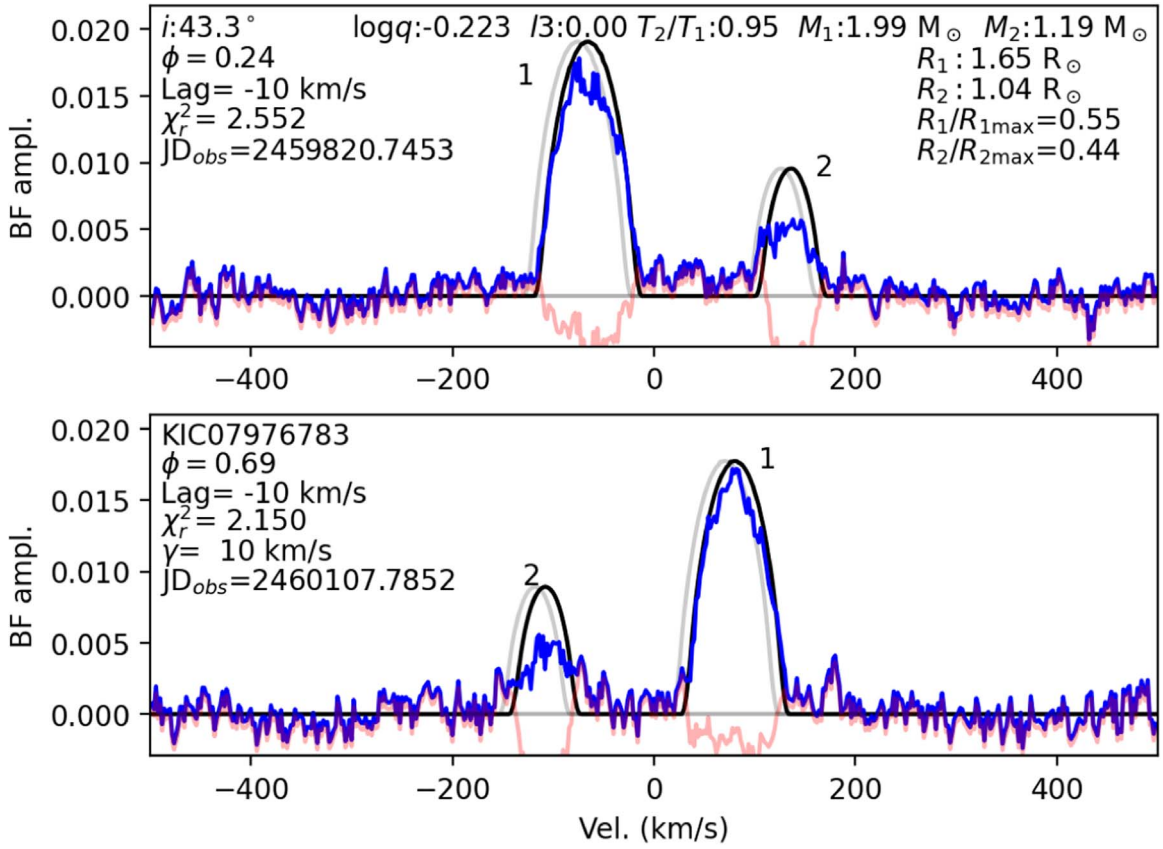

Figure 17. Broadening functions for KIC07976783 (blue lines) with joint PHOEBE fits (black lines) and residuals (salmon lines). The primary and secondary components are marked 1 and 2, respectively.

Table 8
Bayesian 16th, 50th, and 84th Percentile Values for the System Parameters for KIC07884842

	16th	50th	84th
$\cos i$	0.686	0.691	0.696
$\log q$	−0.138	−0.137	−0.136
T_2/T_1	0.904	0.906	0.911
M_1	2.132	2.209	2.229
R_1	1.700	1.712	1.764
R_2/R_1	0.926	0.984	0.999

temperature ratio of $T_2/T_1 = 0.947^{+0.003}_{-0.002}$ and a radius ratio of $R_2/R_1 = 0.627^{+0.008}_{-0.007}$.

4.1.8. KIC07977261

KIC07977261 is a close binary with a period of 0.926 day (Prša et al. 2011). It has a Kepler effective temperature of 6146 K (Prša et al. 2011) and a Gaia effective temperature of 6250 K, indicative of an F7 or F8 primary. Its primary and secondary minima are of significantly different depths, 0.071 and 0.055, respectively. The system shows mirrored changes in the timing of the primary and secondary minima ($\sim \pm 5$ minutes), revealing the presence of drifting starspots. The K22 model for KIC07977261 fit the low amplitude of modulation with an inclination of $i = 27.^{\circ}5^{+2.2}_{-1.8}$ while assigning it a rather middling mass ratio of $q = 0.543^{+0.075}_{-0.069}$.

Figures 19 and 20 show the joint Bayesian fits to the BF and the LC, respectively, as in Figures 4 and 5. Table 10 lists the 50th percentile parameters along with their remarkably symmetric 16th and 84th probability intervals. There is no detectable third light in the BF, consistent with the K22 value of $l3 = 0.11^{+0.12}_{-0.08}$. In contrast to the K22 model for this system, here the shallow minima are explained by a lower mass ratio of $q = 0.262^{+0.013}_{-0.011}$ and a higher inclination of $i = 47.^{\circ}1^{+1.0}_{-1.0}$. While the BF does not at first glance reveal the geometry of KIC07977261, the temperature ratio of $T_2/T_1 = 0.779^{+0.012}_{-0.013}$ exposes the detached nature of the system. However, both components are very near to overfilling their inner Roche surfaces, with $R_1/R_{1\,\max} = 0.95$ and $R_2/R_{2\,\max} = 1.00$. We find that $M_1 = 0.97^{+0.05}_{-0.05}\,M_\odot$ and $R_1 = 2.04^{+0.05}_{-0.04}\,R_\odot$. Taken together with an effective temperature of $\sim$6200 K, the result is a $\sim 1\,M_\odot$ star with a luminosity greater than $5\,L_\odot$. Therefore, we conclude that KIC07977261 is a semidetached system with a post-main-sequence primary. The radius we find for the secondary ($R_2 = 1.15 \pm 0.04\,R_\odot$) is also too large for its nominal main-sequence mass ($M_2 = 0.255 \pm 0.017\,M_\odot$).

4.1.9. KIC08452840

KIC08452840 has a surface temperature in the range 6473–6866 K (Prša et al. 2011; Zhang et al. 2019). It boasts some of the shallowest minima in our sample, with primary and secondary depths of 0.0028 and 0.0017. The ETVs of the primary and secondary minima from Kepler are nothing short of spectacular, showing mirrored shifts in the timing of the primary and secondary minima of over an hour (Balaji et al. 2015), indicating the presence of strong starspot activity. Even once the anticorrelated effects of the starspots are taken out, there is still a trend that appears to repeat every $\sim$1000 days.

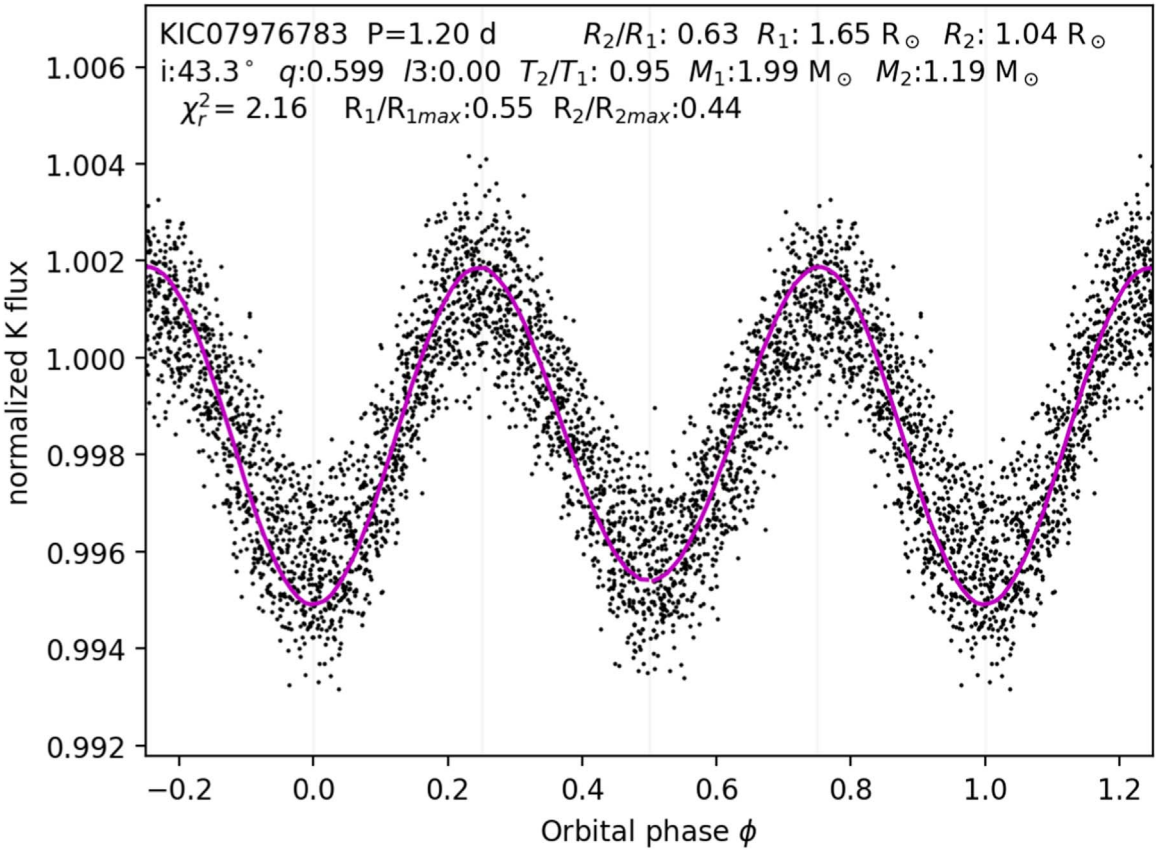

Figure 18. Phase-folded Kepler data for KIC07976783 with the joint fit LC solution (magenta curves).

Table 9
Bayesian 16th, 50th, and 84th Percentile Values for the System Parameters for KIC07976783

	16th	50th	84th
$\cos i$	0.725	0.730	0.734
$\log q$	−0.225	−0.220	−0.215
T_2/T_1	0.945	0.947	0.949
M_1	1.988	1.995	1.998
R_1	1.648	1.658	1.666
R_2/R_1	0.620	0.627	0.635

Additionally, Gaulme & Guzik (2019) found signs of γ Doradus pulsations in this system. The contact model of K22 obtained a mass ratio $q = 0.58^{+0.12}_{-0.11}$, a fillout factor $f = 0.4^{+0.4}_{-0.3}$, and an inclination $i = 7\overset{\circ}{.}3^{+2\overset{\circ}{.}0}_{-1\overset{\circ}{.}0}$. They also obtained a third light fraction $l3 = 0.57^{+0.17}_{-0.22}$, consistent with both the ∼1000 day trend in the ETVs and the Gaia renormalized unit weight error (RUWE[16]) value of 1.8.

Figures 21 and 22 show the joint fit to the BFs and the LC for KIC08452840. Table 11 summarizes the posterior probabilities distributions for the system parameters. We find a temperature ratio of $T_2/T_1 = 0.858^{+0.005}_{-0.005}$, indicating that this system is either a detached binary or semidetached binary. The mass and radius ratios are $q = 0.790^{+0.017}_{-0.016}$ and $R_2/R_1 = 0.918^{+0.010}_{-0.010}$. Unsurprisingly, given the shallowness of the LC minima, the joint fit finds an inclination of $i = 14\overset{\circ}{.}2^{+0\overset{\circ}{.}2}_{-0\overset{\circ}{.}2}$, which leads to large values for the primary mass and radius, $M_1 = 3.986^{+0.010}_{-0.022}\,M_\odot$ and $R_1 = 3.09^{+0.03}_{-0.03}\,R_\odot$. These values correspond to a B9V star, which would have an effective temperature of ∼14,000 K, entirely inconsistent with the range of temperatures given in the literature. Therefore, it is likely that the true orbital inclination is higher than what we find. However, this would require some other parameter to also change in order to fit the shallowness of the LC.

[16] https://gea.esac.esa.int/archive/documentation/GDR2/Gaia_archive/chap_datamodel/sec_dm_main_tables/ssec_dm_ruwe.html

4.1.10. KIC08846978

Coughlin et al. (2011) identified KIC08846978 as an eclipsing binary with an orbital period of 1.379 days and an effective temperature of 5191 K. The system's LC features a prominent O'Connell effect (uneven LC maxima) and unequal primary and secondary minima depths of 0.18 and 0.12, the largest amplitude in our sample by more than a factor of 2. Its sharp shoulders suggest a detached configuration, and substantial changes in both its amplitude and shape indicate significant spot activity. This latter observation is borne out by the system's dramatic anticorrelated ETVs (±1 hr for the timing of the primary minimum; Balaji et al. 2015). This vigorous spot activity resulted in a poor LC fit, leading K22 to classify the system as having an ambiguous geometry with a poorly constrained mass ratio of $q = 0.8^{+1.0}_{-0.5}$. They also find a fillout factor $f = 0.28^{+0.29}_{-0.17}$, an orbital inclination $i = 77^{\circ+10\circ}_{-11\circ}$, and a large third light fraction $l3 = 0.70^{+0.08}_{-0.15}$.

The BF of the system (Figure 23) immediately reveals its detached geometry, which explains the sharp shoulders in the LC (Figure 24). In marked contrast to the high value for third light that K22 found, the BF shows that there is no visible third

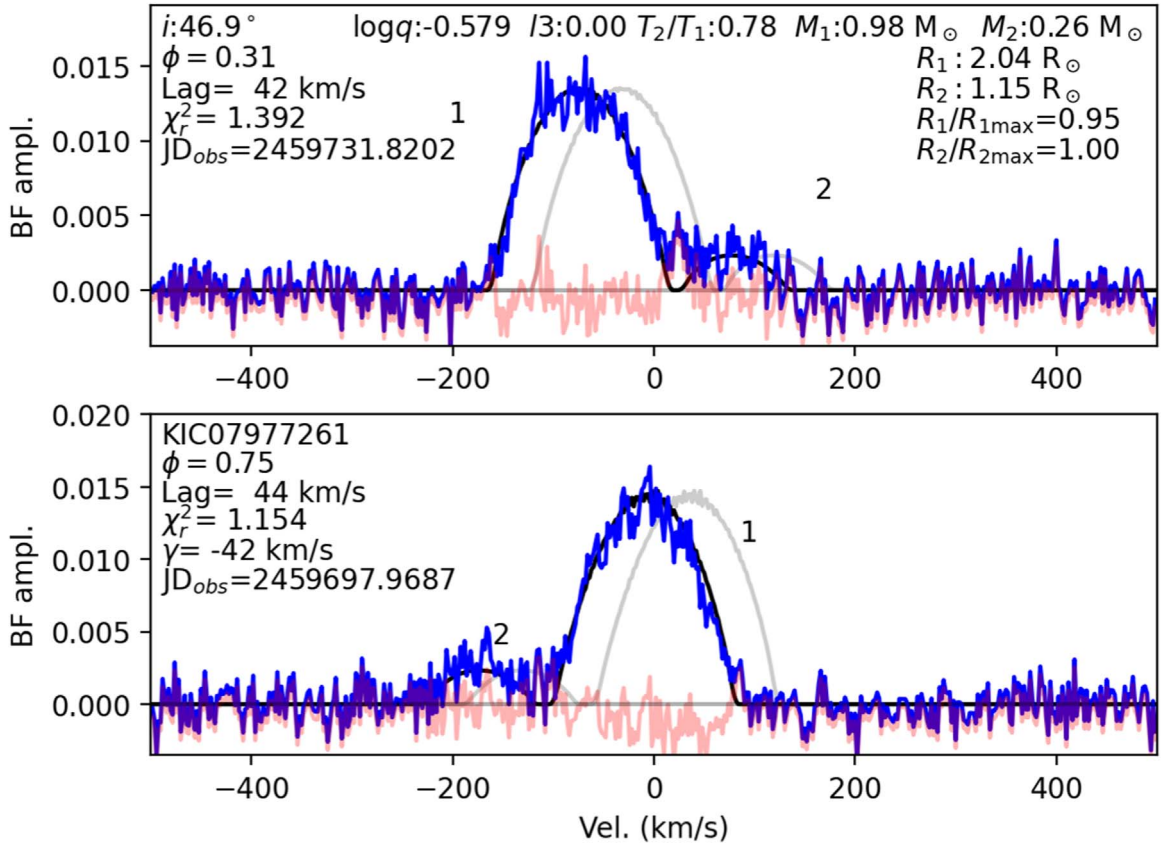

Figure 19. Broadening functions for KIC07977261, as in Figure 4.

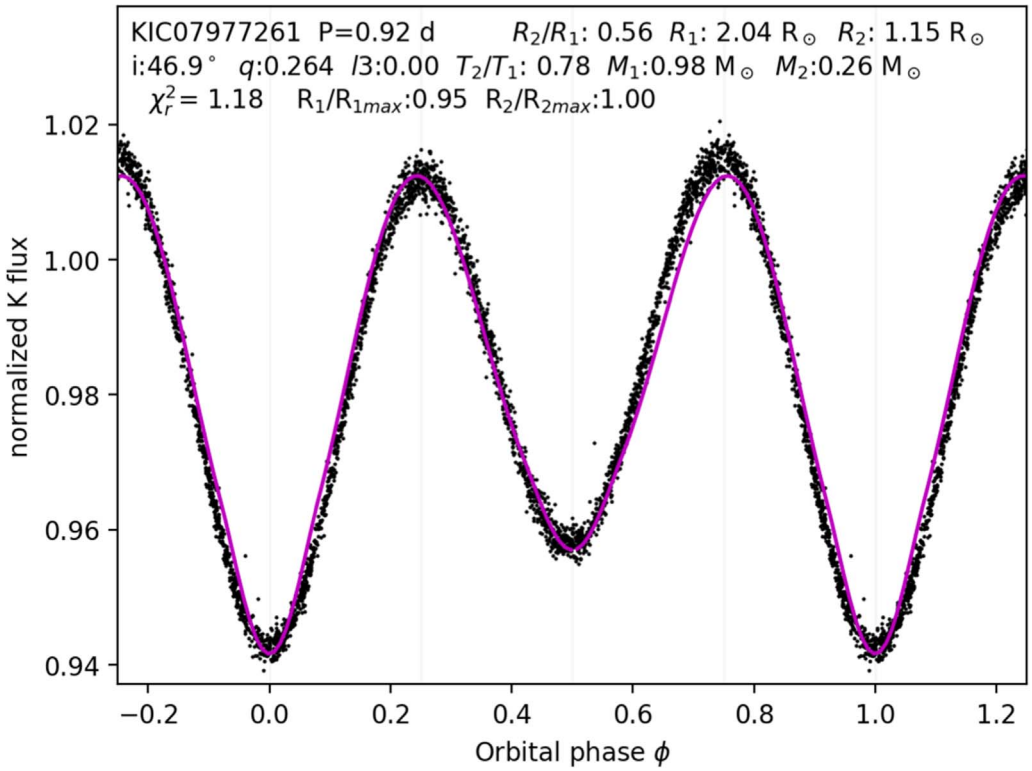

Figure 20. Phase-folded Kepler data for KIC07977261 with the joint fit LC solution (magenta curves), as in Figure 5.

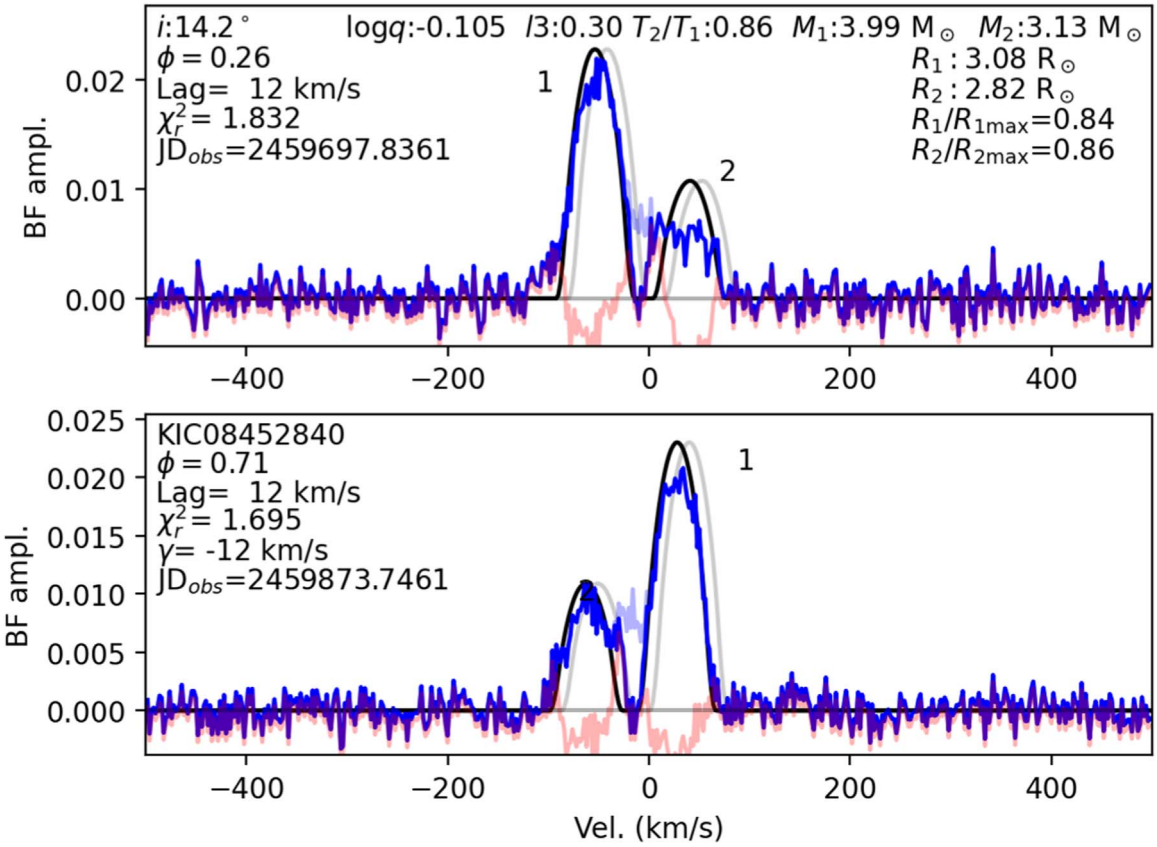

Figure 21. Broadening functions for KIC08452840, as in Figure 4.

Table 10
Bayesian 16th, 50th, and 84th Percentile Values for the System Parameters for KIC07977261

	16th	50th	84th
$\cos i$	0.667	0.680	0.693
$\log q$	−0.602	−0.582	−0.562
T_2/T_1	0.766	0.779	0.791
M_1	0.927	0.973	1.025
R_1	1.997	2.040	2.089
R_2/R_1	0.549	0.562	0.574

light in the system. Table 12 compiles the 16th/50th/84th percentile values for key system parameters. We find a system mass ratio of $q = 0.82^{+0.04}_{-0.04}$ and a systemic velocity of $v_0 = -26\,\mathrm{km\,s^{-1}}$.

The orbital inclination is $i = 63^{\circ+2\circ}_{-2\circ}$, the largest in our sample, which makes sense given the amplitude of the LC and the shape of its eclipses. The temperature ratio ($T_2/T_1 = 0.93^{+0.03}_{-0.03}$) is consistent with the mass ratio, assuming main-sequence stars. The radius ratio is $R_2/R_1 = 1.39^{+0.14}_{-0.14}$, $R_1/R_{1\,\max} = 0.63$, and $R_2/R_{2\,\max} = 0.99$, indicating that this may be a semidetached system. The primary mass and radius are $M_1 = 1.26^{+0.10}_{-0.09}\,M_\odot$ and $R_1 = 1.74^{+0.18}_{-0.17}\,R_\odot$.

4.1.11. KIC09480977

KIC09480977 is a binary with a period of 0.87 day and an effective temperature of 7289 K (Prša et al. 2011). The LC exhibits shallow, unequal minima with depths of 0.0032 and 0.0026 and slightly unequal maxima. It also features variability in the heights and depths of these maxima and minima. The Kepler photometry does not contain any anticorrelated ETVs. Instead, it is likely that the variable amplitude of the LC is due to γ Doradus and δ Scuti pulsations (Gaulme & Guzik 2019). The contact model of K22 ascribed to this system a moderate mass ratio of $q = 0.53^{+0.11}_{-0.12}$, a very low inclination of $i = 16^{\circ+5\circ}_{-3\circ}$, a very large third light fraction of $l3 = 0.84^{+0.07}_{-0.09}$, and a small fillout factor of $f = 0.12^{+0.12}_{-0.05}$.

The motion of the primary component from one quadrature to the next, visible in the BFs in Figure 25, shows that KIC09480977 is a close binary system. However, the secondary is so dim that it is not visible in the BFs, implying an extreme luminosity ratio between the two components. As with KIC05802834, this rules out a contact configuration, in which both components would share a common effective temperature and thus have more similar luminosities. We find a temperature ratio between the two components of $T_2/T_1 = 0.673^{+0.044}_{-0.005}$.

Because the secondary is not visible in the BFs, the parameters relating to it are mainly constrained by the effects of reflected light on the LC (Figure 26). Table 13 compiles the 16th/50th/84th percentile values for key system parameters. In contrast to the contact solution of K22, KIC09480977 contains no discernible third light, and has a relatively extreme mass ratio of $q = 0.211^{+0.010}_{-0.010}$. Similar to K22, our solution entails a very low inclination of $i = 13.^{\circ}5^{+1.^{\circ}1}_{-1.^{\circ}4}$. We find a large primary mass and radius of $M_1 = 2.6^{+0.5}_{-0.7}\,M_\odot$ and $R_1 = 2.4^{+0.3}_{-0.3}\,R_\odot$, and a radius ratio of $R_2/R_1 = 0.43^{+0.03}_{-0.04}$. While the surface temperatures reported in the literature correspond to a late A- or early F-type primary, this mass and radius are consistent with a

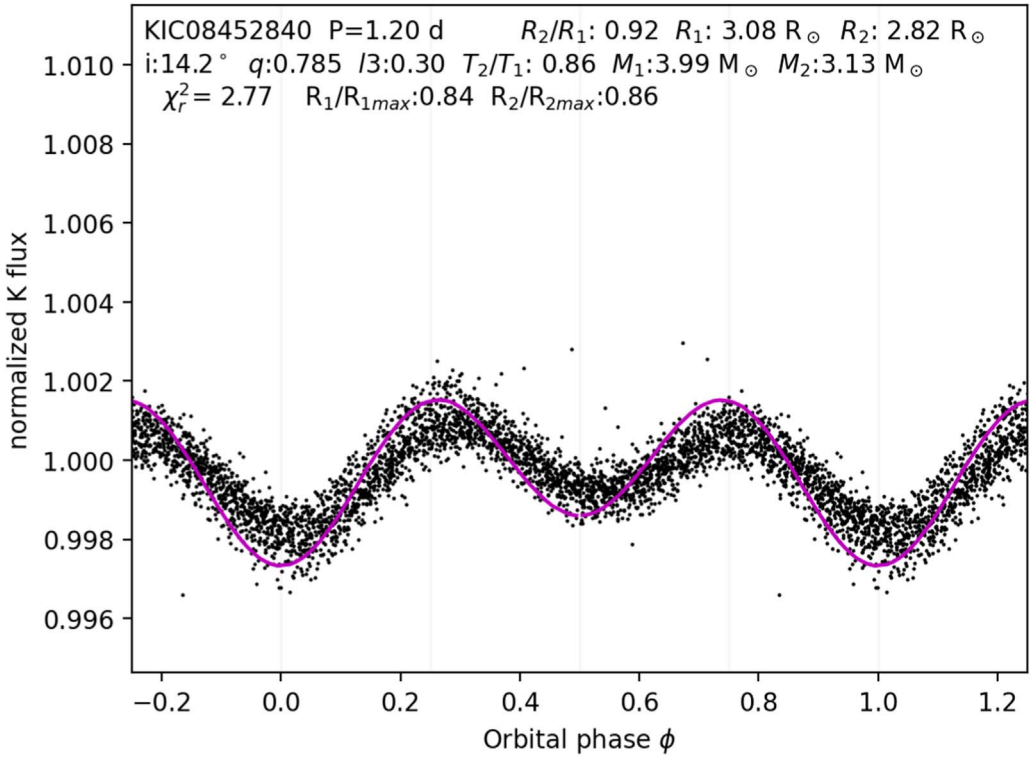

Figure 22. Phase-folded Kepler data for KIC08452840 with the joint fit LC solution (magenta curves), as in Figure 5.

Table 11
Bayesian 16th, 50th, and 84th Percentile Values for the System Parameters for KIC08452840

	16th	50th	84th
$\cos i$	0.969	0.970	0.971
$\log q$	−0.111	−0.102	−0.093
T_2/T_1	0.853	0.858	0.863
M_1	3.964	3.986	3.995
R_1	3.060	3.089	3.118
R_2/R_1	0.908	0.918	0.929

B9.5V primary. However, the uncertainties are large enough to allow for a late-A-type primary.

4.1.12. KIC09602542

KIC09602542 is the most distant target in our sample at $d = 2.6$ kpc. Its effective temperature of 8037 K (Prša et al. 2011) makes it just brighter than our 14th K_p mag cutoff. The primary and secondary minima are of very similar shallow depths, 0.0169 and 0.0171. They also feature small sharp dips at mid-minima, suggesting that the system is an ellipsoidal variable that undergoes a brief grazing eclipse. The system's ETVs show that the primary minimum is consistently 5 minutes tardy, suggesting either a stationary spot or a slightly eccentric orbit. While recognizing the binary nature of the source, Balona (2018) additionally lists this system as exhibiting δ Scuti pulsations, and Gaulme & Guzik (2019) catalogs it as both a δ Scuti and a γ Doradus variable. The K22 contact model explains the shallow eclipses using a low inclination of $i = 45^{\circ+3\circ}_{-4\circ}$ and a very large third light fraction of $l3 = 0.87^{+0.02}_{-0.03}$. Additionally, they find a mass ratio very near unity of $q = 0.98^{+0.22}_{-0.15}$ and a low fillout factor of $f = 0.13^{+0.09}_{-0.06}$.

The BF shown in Figure 27 unambiguously reveals that KIC09602542 is a detached system. This explains why the contact model from K22 settled on a rather small fillout factor and required large third light and a lower inclination to reproduce the shallow minima. In contrast to the K22 results, the system contains no discernible third light and has an orbital inclination of $i = 67^{\circ+2\circ}_{-3\circ}$. The low amplitude of modulation in the LC in Figure 28 is due to the detached geometry of the system. The system velocity is $-40\,\mathrm{km\,s^{-1}}$. As shown in Table 14, our detached model yields values for the mass, radius, and temperature ratios of $q = 0.080^{+0.015}_{-0.011}$ (the most extreme in our sample), $R_2/R_1 = 0.55^{+0.03}_{-0.04}$, and $T_2/T_1 = 0.983^{+0.011}_{-0.010}$. The radius and temperature ratios are much higher than one would expect from two main-sequence stars with such an extreme mass ratio. We obtain a primary mass and radius of $M_1 = 1.76^{+0.13}_{-0.19}\,M_\odot$ and $R_1 = 1.76^{+0.12}_{-0.15}\,R_\odot$, and a secondary mass and radius of $M_2 = 0.14 \pm 0.02\,M_\odot$ and $R_2 = 0.97 \pm 0.10\,R_\odot$. These masses, radii, and the Kepler effective temperature given above are all consistent with a A5V main-sequence primary having a much less-massive (but bloated) secondary (Pecaut & Mamajek 2013). It remains unclear how the secondary could have a temperature as high as 0.98 that of the primary.

4.1.13. KIC10789421

KIC10789421 is a close binary with an orbital period $P = 0.777$ day, an effective temperature of $T_{\rm eff} = 7137$ K, and a spectral type of F1V (Frasca et al. 2016). The system's Kepler LC reveals very shallow, unequal minima (0.005 and 0.003), unequal maxima, and significant changes in the depths of the minima. The shallowness and unevenness of the minima suggest that the system could be a detached ellipsoidal variable with a T_2/T_1 different from unity. The ETVs for primary and

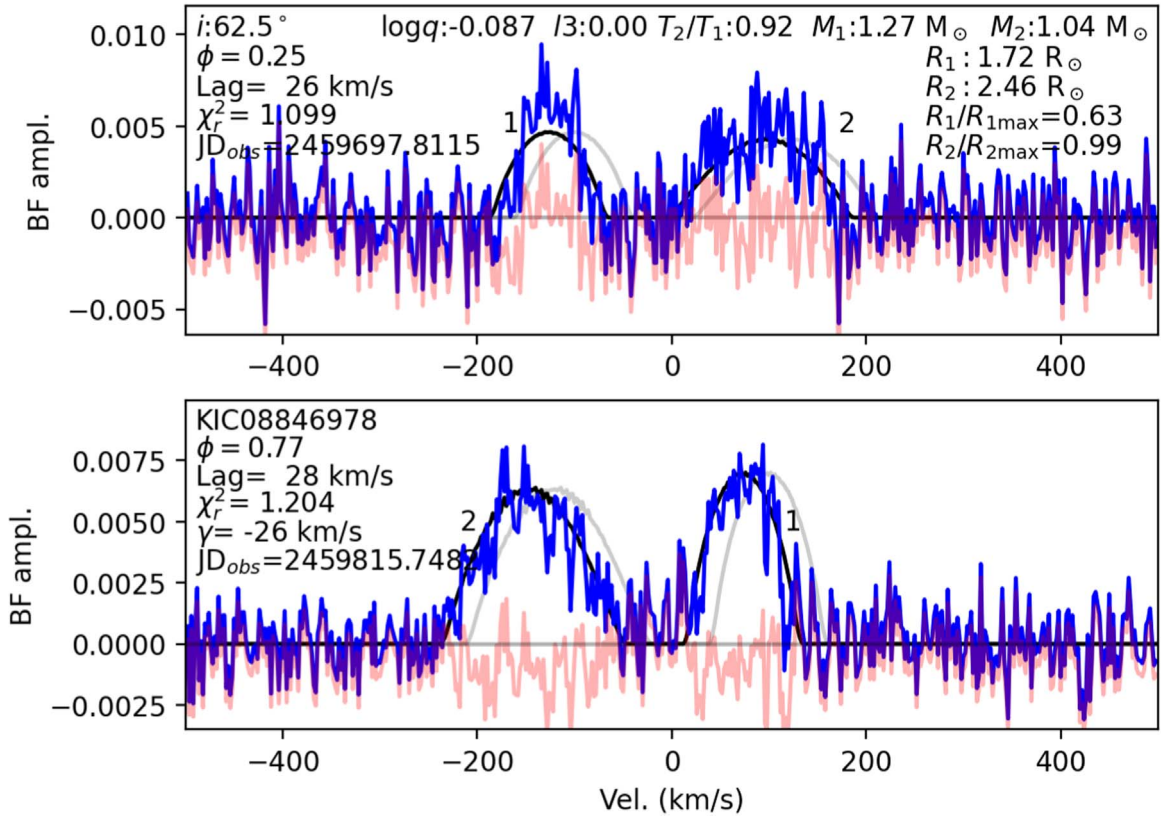

Figure 23. Broadening functions for KIC08846978, as in Figure 4.

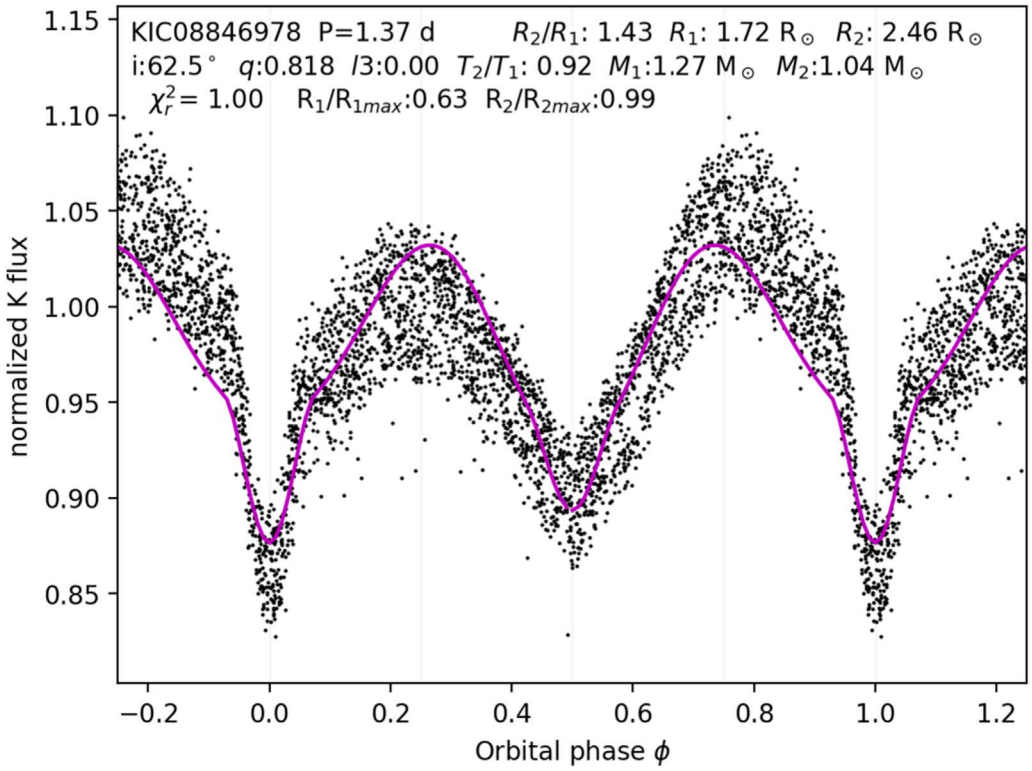

Figure 24. Phase-folded Kepler data for KIC08846978 with the joint fit LC solution (magenta curves), as in Figure 5.

secondary minimum show a repeating, anticorrelated pattern with a period of $P_{\rm ETV} \approx 400$ days and amplitude of approximately 15 minutes, indicating the presence of spots in the system. In addition to being a binary, Gaulme & Guzik (2019) claimed that it exhibits γ Doradus pulsations. K22 found a mass ratio of $q = 0.60^{+0.09}_{-0.07}$. They explained the shallow

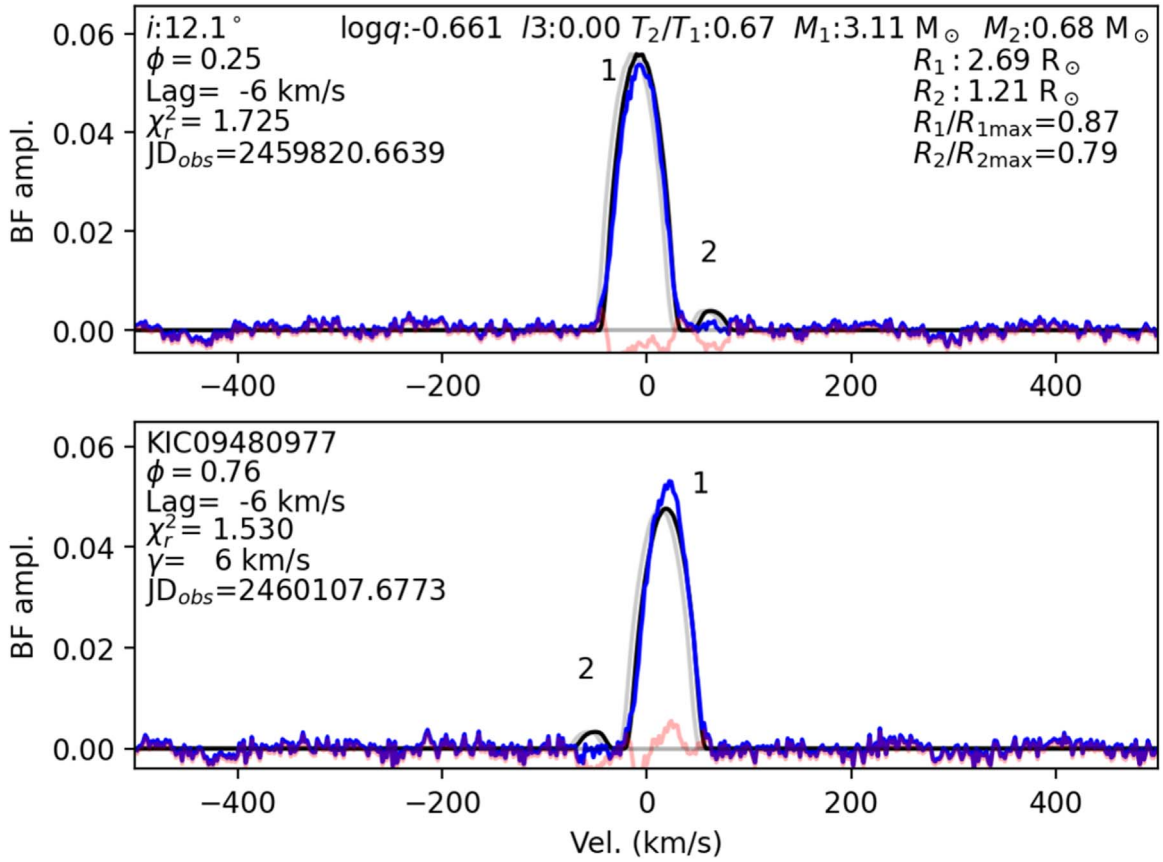

Figure 25. Broadening functions for KIC09480977, as in Figure 4.

Table 12
Bayesian 16th, 50th, and 84th Percentile Values for the System Parameters for KIC08846978

	16th	50th	84th
$\cos i$	0.426	0.458	0.491
$\log q$	−0.107	−0.087	−0.067
T_2/T_1	0.903	0.928	0.958
M_1	1.162	1.257	1.358
R_1	1.578	1.745	1.928
R_2/R_1	1.248	1.385	1.524

minima with a contact model having a very low inclination of $i = 8.^{\circ}9^{+0.^{\circ}7}_{-0.^{\circ}8}$, a moderate third light fraction of $l3 = 0.29^{+0.11}_{-0.04}$, and a fillout factor of $f = 0.24^{+0.35}_{-0.17}$.

As can be seen in the BF in Figure 29, the two components evince vastly different heights, which we here explain using a detached model with a temperature ratio of $T_2/T_1 = 0.742^{+0.008}_{-0.010}$ and a radius ratio of $R_2/R_1 = 0.543^{+0.007}_{-0.009}$. Along with our value for the inclination of $i = 17.^{\circ}9^{+0.^{\circ}6}_{-0.^{\circ}6}$, this explains the shallow, unequal minima in the system's LC (Figure 30). Table 15 compiles the 16th/50th/84th percentile values for key system parameters. The difference in luminosities of the two components is large enough that we used a 6000 K stellar template when producing the BFs in order to enhance the signal of the fainter, cooler secondary. While the model of K22 was correct in resorting to a low inclination to explain the LC, we obtain a very different value for the mass ratio, $q = 0.195^{+0.006}_{-0.006}$. The primary mass and radius are $M_1 = 1.16^{+0.04}_{-0.10}\,M_{\odot}$ and $R_1 = 1.63^{+0.04}_{-0.06}\,R_{\odot}$. The absence of third light in the system means that the cyclic ETVs are likely due to starspots rather than a third body. The system parameters are consistent with a close detached binary with an F-type primary and an M-type secondary.

4.2. Other Variables

Our sample of 18 putative close binaries contains five systems that turn out to be either rotating (four systems) or pulsating variables (one system). Their primary and secondary minima in the Kepler LCs have essentially equal depths, indicating that their true periods could be half their putative binary orbital periods. None of these systems' LCs exhibit anticorrelated ETVs. Some of them do have large, random ETVs, as one would expect from spotted rotators. All have very shallow LC minima ($\lesssim$1%) except for KIC05196301, which has LC modulations of over 5%.

We extracted values for the projected rotational velocities and the radial velocities by deconvolving these peaks with a narrow Gaussian representing the instrumental profile, then fitting analytical rotation curves for single stars (Gray 2005) to the deconvolved BFs. Table 16 gives the KIC numbers, the projected rotational velocities $v_{\rm R}\sin i$, the radial velocities, the number of observations, the period, the amplitude of LC modulation, and the effective temperature. Figure 31 shows a representative BF for each system. They range from very narrow ($v_{\rm R}\sin i = 7.26 \pm 0.07\,{\rm km\,s^{-1}}$) to very broad ($v_{\rm R}\sin i = 82.0 \pm 0.7\,{\rm km\,s^{-1}}$). All are single-peaked except for KIC08386865.

The BFs of KIC01295531 contain a single, unmoving peak at $v_{\rm rad} = -12$ km s^{-1} with $v_{\rm R}\sin i = 25.02 \pm 0.10\,{\rm km\,s^{-1}}$.

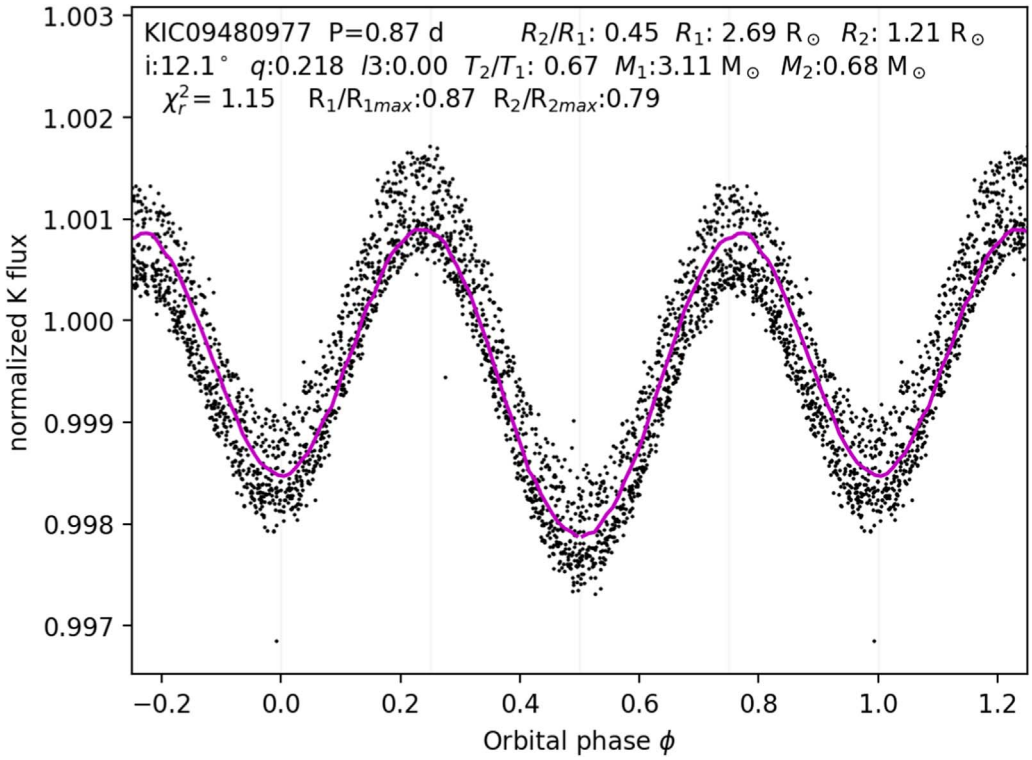

Figure 26. Phase-folded Kepler data for KIC09480977 with the joint fit LC solution (magenta curves), as in Figure 5.

Table 13
Bayesian 16th, 50th, and 84th Percentile Values for the System Parameters for KIC09480977

	16th	50th	84th
$\cos i$	0.968	0.972	0.978
$\log q$	−0.695	−0.675	−0.655
T_2/T_1	0.668	0.673	0.717
M_1	1.901	2.558	3.079
R_1	2.172	2.425	2.681
R_2/R_1	0.394	0.432	0.464

This projected rotational speed is consistent with the expected rotation rate of a mid-F-type star (Nielsen et al. 2013). The stationary nature of the peak implies that the LC modulation is due to either pulsations or spots. The system's large, random ETVs argue strongly for the latter. Therefore, we come to the same conclusion as Reinhold et al. (2013): KIC01295531 is a rotating variable with a period of 0.84 day.

KIC05196301 has an effective temperature of ∼4700 K. Taken together with its parallactic distance (235 pc) and its apparent magnitude, this system is consistent with an early- to mid-K dwarf. It has a radial velocity of $v_{\rm rad} = -32\,{\rm km\,s^{-1}}$, which remains constant from what would be one quadrature to the next, if the system were a contact binary. This implies that it is either a pulsating or rotating variable. Its large, random ETVs favor the latter. However, the latter would imply a rotation period of 0.96 day, a factor of 10 smaller than expected for an early- to mid-K dwarf. In either case, the projected rotation velocity of $v_{\rm R} \sin i = 39.7 \pm 0.3\,{\rm km\,s^{-1}}$ is about a factor of 10 larger than typical K dwarfs (Nielsen et al. 2013). This rapid rotation is likely to give rise to enhanced magnetic activity and intense spot variability. The presence of spots is further supported by the fact that the changes in the depths of the minima over time are similar to the depths of the minima themselves. Under the assumption that the LC modulation period is the rotation period of the star, the projected rotational velocity yields a lower limit on the radius of the star $R \gtrsim 0.75\,R_\odot$, which is also consistent with an early- to mid-K dwarf. The Gaia RUWE value for this system is 4.4, which could indicate a nonsingle source. However, the BFs exhibit no secondary peak, regardless of the temperature of the stellar template used to produce them. We conclude that KIC05196301 is an anomalously rapidly rotating K dwarf whose LC modulations arise from the presence of large and variable starspots.

KIC05386810 has a remarkably uncertain effective temperature, with values in the literature ranging from 7395 K (Prša et al. 2011) to 8534 K (Zhang et al. 2019). Its BFs show a single peak near $v_{\rm rad} = -20\,{\rm km\,s^{-1}}$. The narrowness of the peak ($v_{\rm R} \sin i = 7.26 \pm 0.07\,{\rm km\,s^{-1}}$) suggests that we are viewing the star at a low inclination, which would be consistent with the very small LC modulation under the assumption it is a rotating variable. Balona (2019) measured that the spin period is equal to the period of LC modulation. Additionally, the ETVs evince large, random changes, consistent with the presence of vigorous starspot activity. Therefore, we conclude that KIC05386810 is a rotating variable.

The BF of KIC08386865 features a broad component at $v_{\rm rad} = 9.6 \pm 0.5\ {\rm km\,s^{-1}}$ and a narrow secondary peak at $v_{\rm rad} \approx -10\,{\rm km\,s^{-1}}$. These radial velocities are constant within the uncertainties over a time baseline of 4 months. Using a cooler template spectrum to produce the BFs causes the secondary peak to become more pronounced, indicating that it is cooler than the primary. The system's ETVs show a repeating pattern with a full amplitude of ∼8 minutes and a period of ∼300 days. If the source of the LC modulation is the secondary, then the ETVs are naturally explained by the light

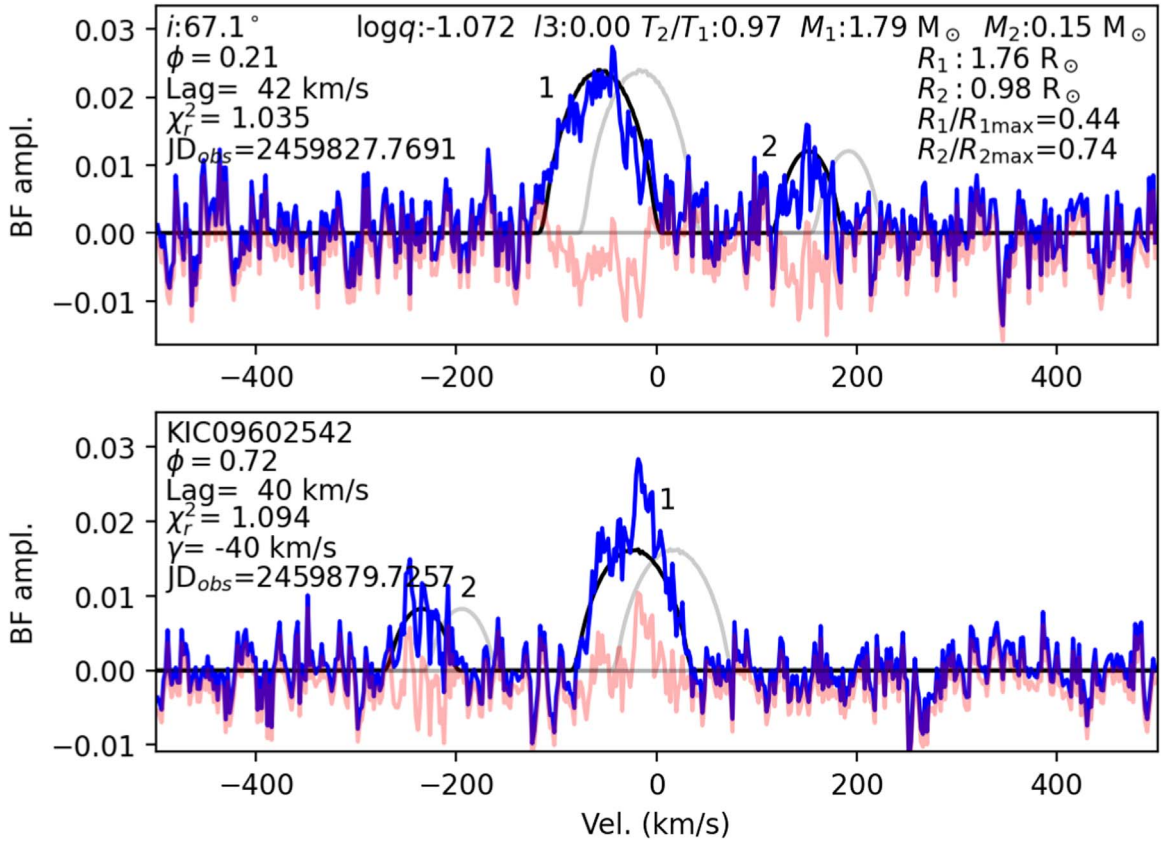

Figure 27. Broadening functions for KIC09602542, as in Figure 4.

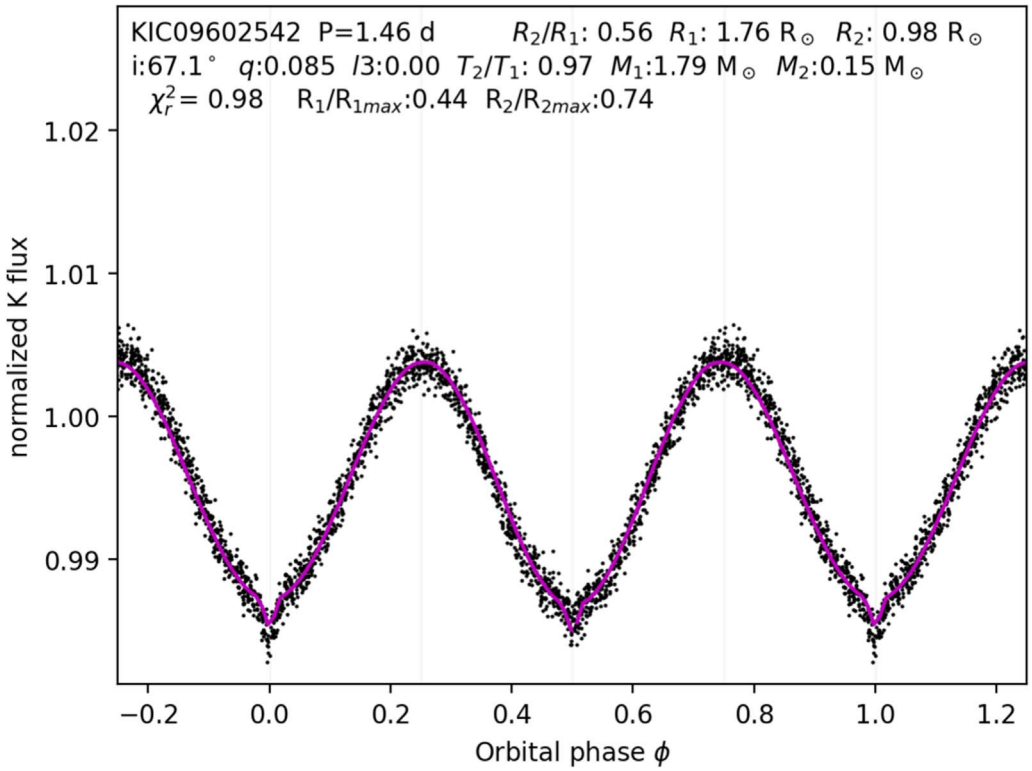

Figure 28. Phase-folded Kepler data for KIC09602542 with the joint fit LC solution (magenta curves), as in Figure 5.

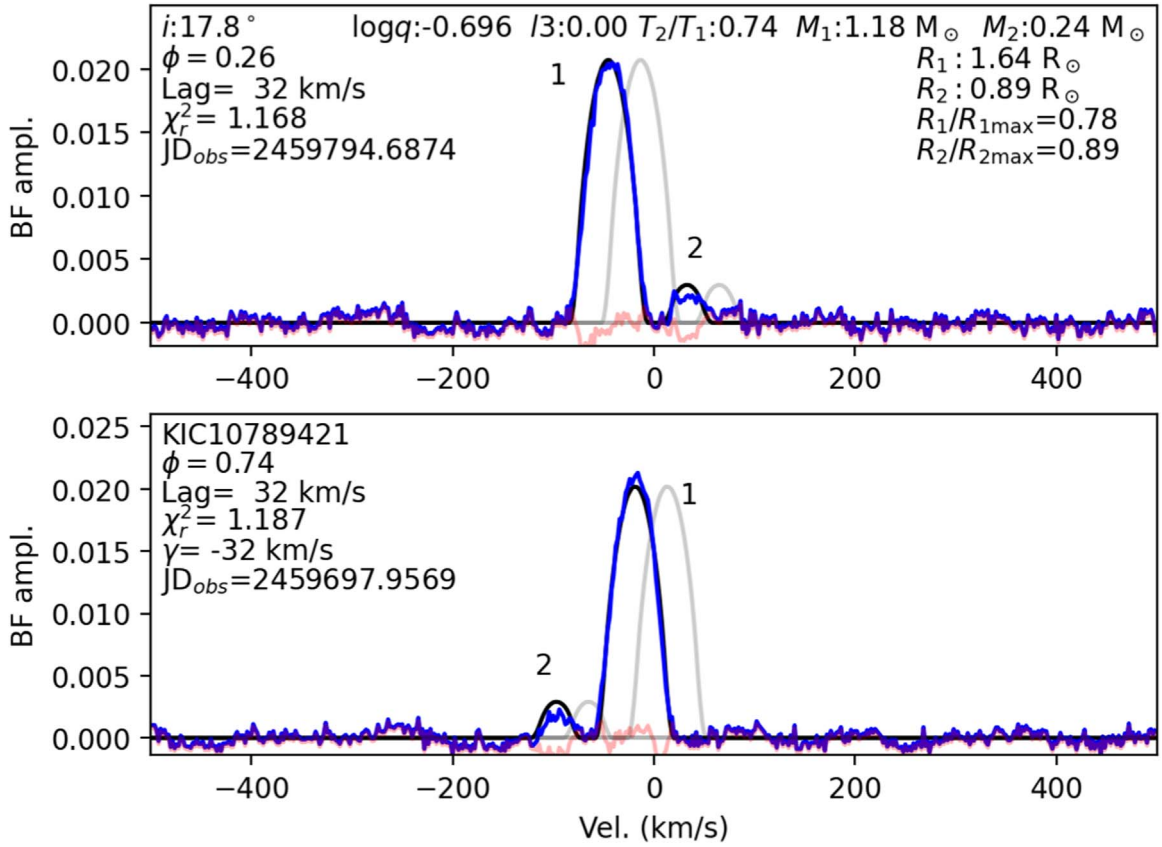

Figure 29. Broadening functions for KIC10789421, as in Figure 4.

Table 14
Bayesian 16th, 50th, and 84th Percentile Values for the System Parameters for KIC09602542

	16th	50th	84th
$\cos i$	0.367	0.395	0.439
$\log q$	−1.163	−1.095	−1.021
T_2/T_1	0.972	0.983	0.993
M_1	1.571	1.757	1.884
R_1	1.608	1.757	1.881
R_2/R_1	0.510	0.549	0.580

travel time effects of an eccentric orbit with $a \sin i \approx 4$ light minutes ≈0.5 au. Given the narrowness of the secondary in the BFs, the 0.63 day 1% amplitude LC modulations are best explained by the secondary being a pulsating variable. In summary, the evidence points to KIC08386865 being an eccentric binary consisting of a rapidly rotating A-type primary with $v_R \sin i = 82.0 \pm 0.7$ km s^{-1} and a cooler, pulsating secondary with a projected rotational velocity of $v_R \sin i \approx 6$ km s^{-1}. Gaia Collaboration (2022) also recently cataloged this system as containing a pulsating variable.

Our BF for KIC08451777 reveals a single peak with a radial velocity of $v_{rad} = -5$ km s^{-1}. Its surface temperature of 6752 K and its projected rotation velocity of $v_R \sin i = 47.6 \pm 0.8$ km s^{-1} are both consistent with an early- to mid-F dwarf. The period of its LC is 1.52 days (Nielsen et al. 2013). Assuming that this is the rotation period of the star, the projected rotational velocity supplies a lower limit on the star's radius of $R \gtrsim 1.43\,R_\odot$, which is also consistent with a mid-F dwarf. This suggests that the period of modulation of the system's light is the stellar rotation period. Therefore, we agree with Nielsen et al. (2013) that KIC08451777 is a rotating variable.

5. Discussion

5.1. Testing M22 Contact Binary Evolution Models

The third-light fraction and mass ratio are key parameters for testing contact binary formation and evolutionary models. Thus, BFs prove to be invaluable in testing such models, because they afford direct measurement of both q and $l3$, even at low inclinations. Due to the photometric degeneracies between q, $l3$, and i, LCs alone typically lack such power. However, determination of system mass is also required to fully test evolutionary models, and this requires more information on i than is encoded in BFs alone. Therefore, combining the information in systems' LCs and BFs is the ideal way to retrieve all relevant system parameters in order to test models for contact binary evolution and formation.

Consistent with the predictions made by the M22 evolutionary tracks, all of the close binaries in our sample turn out to be detached or semidetached, with the exception of KIC07766185. It has mass ratio $q = 0.8$, orbital period $P = 0.835$ day, and total system mass $M_{tot} = 3.2\,M_\odot$. Because its higher mass indicates it has a radiative envelope ($M_{tot} \leqslant 2.47\,M_\odot$), this system does not provide a test of the M22 evolutionary tracks (L. Molnar 2023, private communication). Therefore, none of these systems constitutes a violation of the M22 evolutionary scenario.

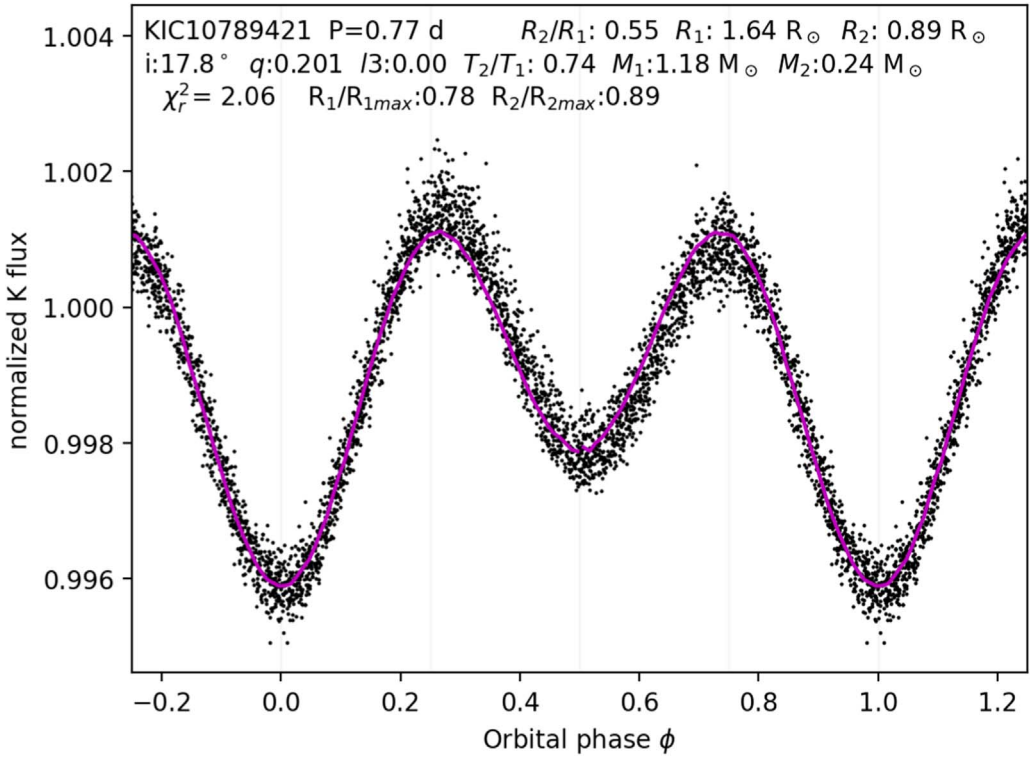

Figure 30. Phase-folded Kepler data for KIC10789421 with the joint fit LC solution (magenta curves), as in Figure 5.

Table 15
Bayesian 16th, 50th, and 84th Percentile Values for the System Parameters for KIC10789421

	16th	50th	84th
$\cos i$	0.948	0.952	0.955
$\log q$	−0.725	−0.711	−0.697
T_2/T_1	0.731	0.742	0.749
M_1	1.059	1.163	1.202
R_1	1.572	1.629	1.670
R_2/R_1	0.534	0.543	0.550

Table 16
Rotating Variables and Other Variables

KIC	$v_R \sin i$ (km s^{-1})	v_{rad} (km s^{-1})	N_{obs}	P (days)	*pdepth*	T_{eff} (K)
01295531	25.02± 0.10	−12	4	0.84	0.0097	7177
05196301	39.7 ± 0.3	−32	2	0.96	0.0585	4710
05386810	7.26 ± 0.07	−20	2	0.44	0.0006	8074
08386865	82.0 ± 0.7	10	3	0.63	0.0113	9002
08451777	47.6 ± 0.8	−5	1	1.52	0.0012	6752

Note. Effective temperatures are from Gaia (Gaia Collaboration et al. 2023), except for KIC08451777, where it comes from Frasca et al. (2016).

5.2. Analysis of System Parameters

Table 17 summarizes our results for the 18 systems in our sample (KIC numbers in column 1), along with their periods (column 2), and effective temperatures (column 3). Columns 4–13 show the best-fitting parameters for q, R_2/R_1, T_2/T_1, i, M_1, R_1, $\log g_1$, $\log g_2$, $R_1/R_{1\,max}$, and $R_2/R_{2\,max}$, respectively. Column 14 shows our diagnosis for the type or geometry of each system.

Four of the 12 noncontact binaries in our sample are semidetached (SD), specifically, with the secondary filling its Roche lobe. Even for the eight detached binaries (D), the secondary radii are larger than main-sequence mass–radius relations would predict. Figure 32 plots the stellar radii versus masses for both the primaries (blue circles) and the secondaries (orange diamonds) in the 12 noncontact systems, illustrating this trend. The black line traces radii and masses from the Pecaut & Mamajek (2013) compilation[17] of main-sequence stellar parameters. While the primaries generally straddle the main-sequence mass–radius relationship, the secondaries tend to fall above it, indicating that secondaries in these close noncontact binaries are consistently bloated. One possible explanation is that the secondaries are bloated because of radiative heating from their hotter primaries.

Figure 33 plots T_2/T_1 against $\log q$ for the 12 noncontact systems. The dashed line, the dashed–dotted line, and the dotted line trace the expected T_2/T_1–$\log q$ relationships for detached binaries with main-sequence components. We calculated these MS expectations using the results of Pecaut & Mamajek (2013) for systems with G0V, F0V, and A0V primaries, respectively. The solid line shows the best exponential fit to our results, $T_2/T_1 \propto q^{0.21}$, which falls significantly above the expected main-sequence relations. This provides additional support for the idea that the primaries are heating the secondaries. When making the same plot using the detached fits to the 114 probable detached systems from K22, there is a small hint of a reasonable trend, but the plot mostly shows random scatter. This underscores that LCs alone cannot reliably constrain key parameters for detached systems, even when the system geometry is known.

[17] https://www.pas.rochester.edu/~emamajek/EEM_dwarf_UBVIJHK_colors_Teff.txt

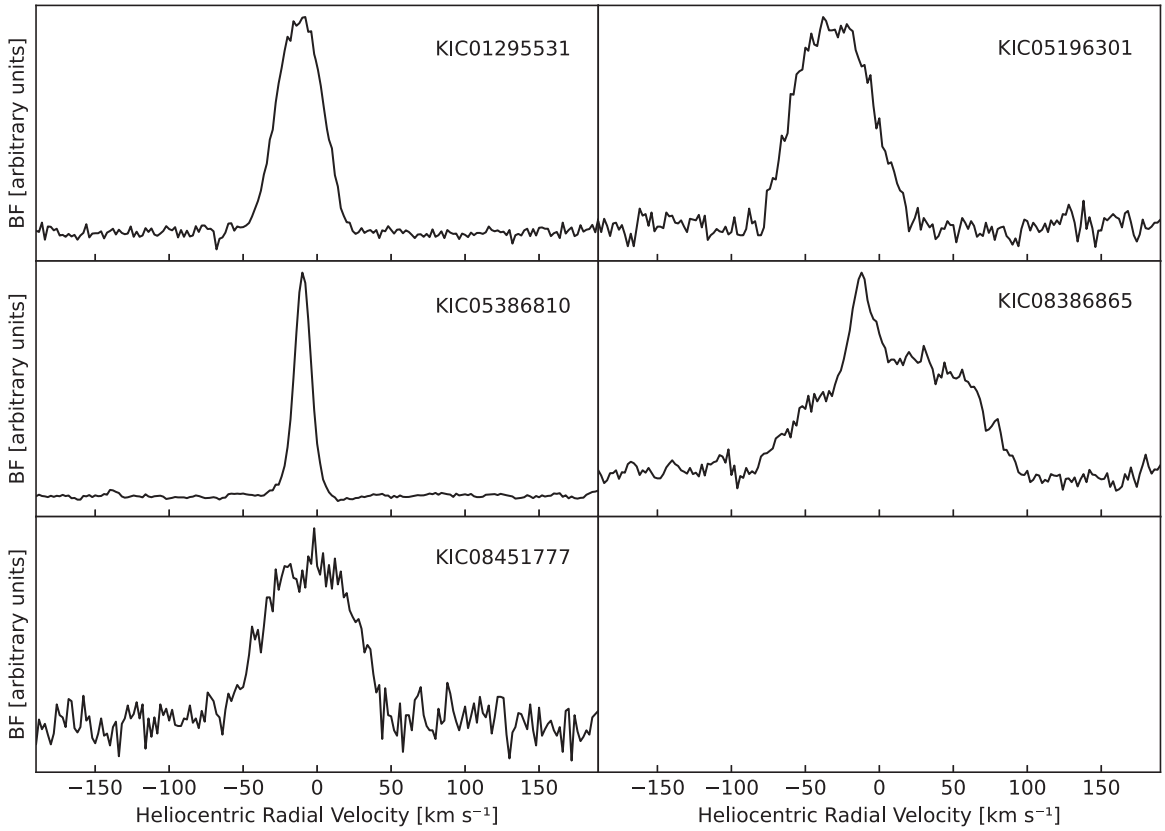

Figure 31. Representative BFs of the five nonbinary variables.

Table 17
Summary of Best-fitting Parameters

KIC ID	P (days)	$T_{\rm eff}$ (K)	q	R_2/R_1	T_2/T_1	i (°)	M_1 ($M_\odot$)	R_1 ($R_\odot$)	$\log g_1$	$\log g_2$	$\frac{R_1}{R_{1\,\max}}$	$\frac{R_2}{R_{2\,\max}}$	Type
(1)	(2)	(3)	(4)	(5)	(6)	(7)	(8)	(9)	(10)	(11)	(12)	(13)	(14)
01295531	0.843	6567[a]											R
04954113	0.668	7730[b]	0.452	0.81	0.76	36.9	1.73	1.67	4.23	4.08	0.84	1.00	SD*
05196301	0.955	4546[c]											R
05386810	0.444	7395[c]											R
05802834	1.092	6077[c]	0.253	0.59	0.71	48.0	1.77	0.45	4.27	3.88	0.85	0.94	D
06670812	1.742	6403[d]	0.875	0.72	1.01	54.6	1.27	1.95	4.11	4.24	0.61	0.47	D*
06692340	0.675	6270[c]	0.614	0.83	0.86	15.9	1.69	1.04	4.13	4.10	0.95	1.00	SD
07766185	0.835	6437[a]	0.821	0.91	0.96	74.3	1.68	2.17	3.99	3.99			C
07884842	1.315	9126[c]	0.731	1.00	0.91	46.0	2.23	1.70	4.03	4.09	0.53	0.61	D
07976783	1.209	8071[a]	0.599	0.63	0.95	43.3	1.99	1.65	4.30	4.27	0.55	0.44	D
07977261	0.926	6910[b]	0.264	0.56	0.78	46.9	0.98	2.04	3.99	3.59	0.95	1.00	SD
08386865	0.629	9226[b]											P*
08451777	1.515	6752[a]											R
08452840	1.201	6606[a]	0.785	0.92	0.86	14.2	3.99	3.08	4.60	4.69	0.84	0.86	D*
08846978	1.379	5680[e]	0.818	1.43	0.92	62.5	1.27	1.72	4.10	4.20	0.63	0.99	SD
09480977	0.871	7357[a]	0.218	0.45	0.67	12.1	3.11	2.69	4.41	3.92	0.87	0.79	D
09602542	1.463	7899[a]	0.085	0.56	0.97	67.1	1.79	1.76	4.25	3.34	0.44	0.74	D
10789421	0.777	7137[a]	0.201	0.55	0.74	17.8	1.18	1.64	4.07	3.54	0.78	0.89	D

Notes. D—detached; SD—semidetached; C—contact; R—rotating variable; P—pulsating variable; *—BF shows an additional narrow component.
[a] Frasca et al. (2016).
[b] Zhang et al. (2019).
[c] Prša et al. (2011).
[d] Casagrande et al. (2011).
[e] Qian et al. (2018).

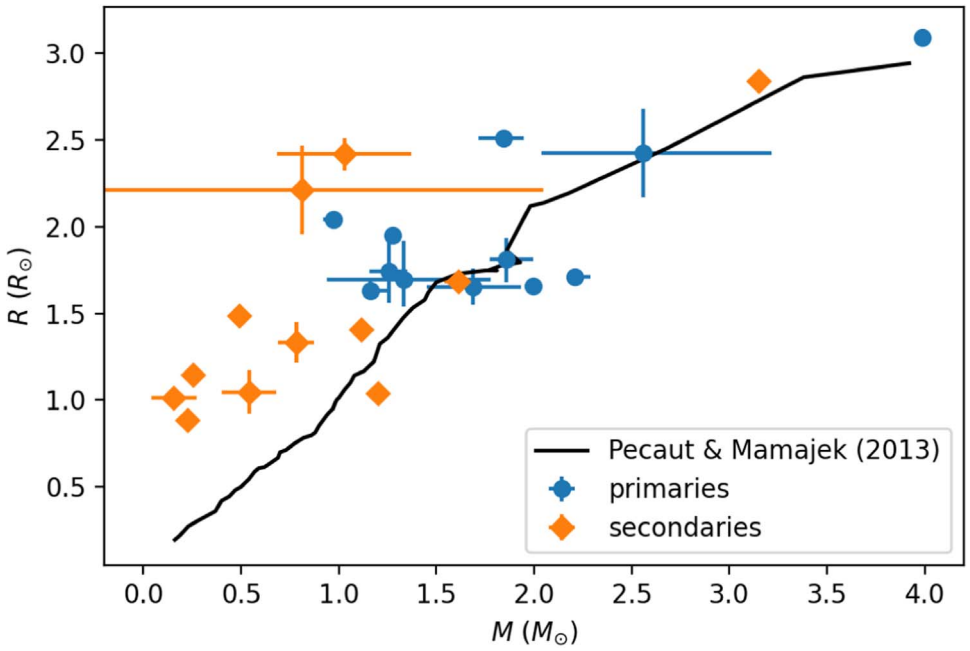

Figure 32. Radius vs. mass (50th percentile values) for both the primaries (blue dots) and the secondaries (orange diamonds) in the 12 noncontact binaries. The error bars stretch to the 16th and 84th percentile values. The black line shows an empirical MS mass–radius relation.

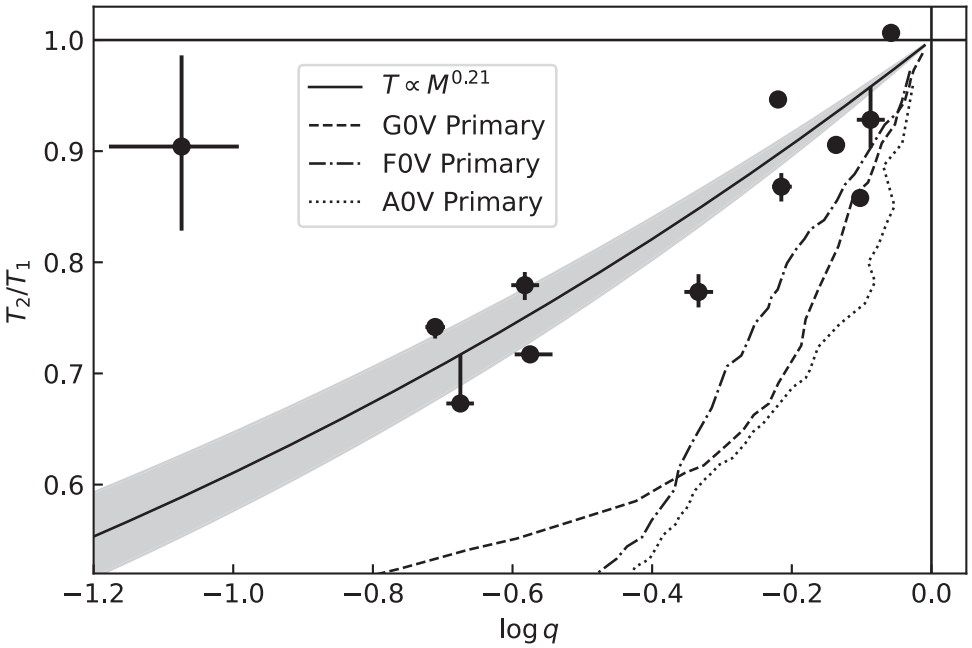

Figure 33. T_2/T_1 vs. $\log q$ for the 12 noncontact binaries, using the 50th percentile parameters. The error bars stretch to the 16th and 84th percentile values. The solid line with the gray uncertainty intervals show the best exponential fit to the results. The dashed, dashed–dotted, and dotted lines show the empirical MS T_2/T_1–$\log q$ relations for binaries with G0V, F0V, and A0V primaries, respectively.

We find that most of the values of $\log g_1$ and $\log g_2$ in Table 17 are consistent with main-sequence expectations. The primary surface gravities fall in the range $4.0 \lesssim \log g_1 \leqslant 4.3$, with the exception of KIC08452840 and KIC09480977, which have uncomfortably high values for $\log g_1$ given the primary masses we obtain. A possible resolution for these two systems is the uncertainty on third light fraction. The uncertainty on $l3$ in both of these systems should affect the uncertainty on the inclinations given the very low amplitude of both light curves, but that is not reflected in the reported uncertainties because third light was removed before the joint-fitting process.[18] It is possible that the full uncertainty on the inclinations of these two systems would be enough to bring their values for $\log g$ into agreement with main-sequence expectations. The

[18] To include third light fitting in the joint-fitting procedure would involve introducing a number of additional free parameters, making the study much more computationally expensive.

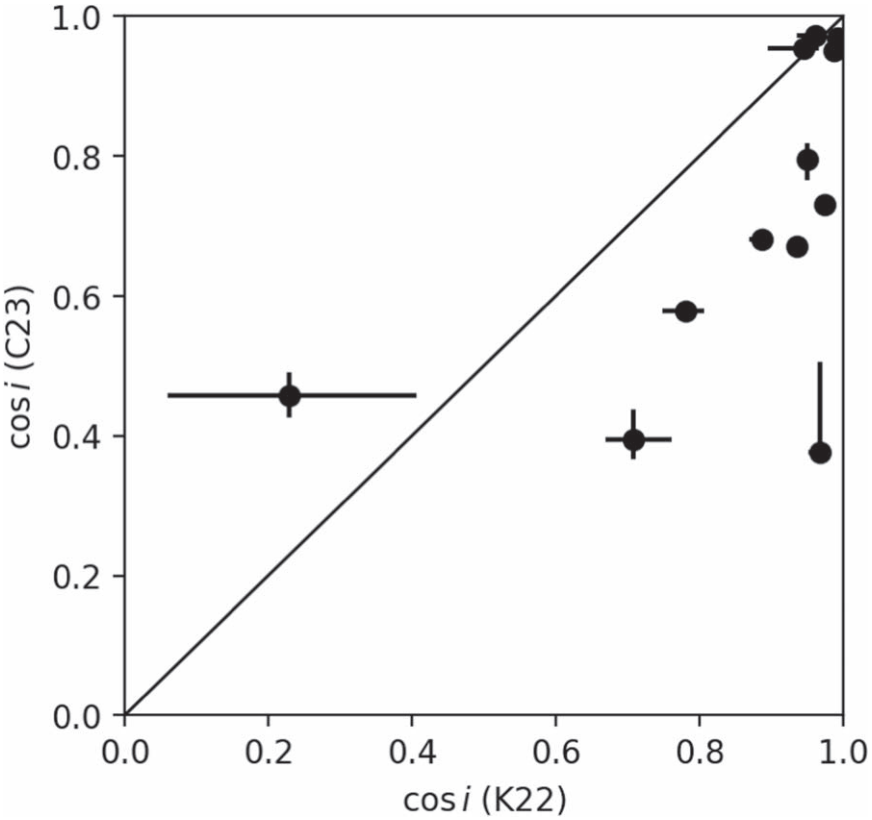

Figure 34. A comparison between the orbital inclinations found by the K22 contact solutions and the values we obtain for the 12 noncontact systems.

secondaries' values for $\log g$ also mostly fall in line with main-sequence expectations or slightly lower by 0.1–0.2 dex, with the exceptions of KIC08452840, KIC07977261, KIC09602542, and KIC10789421. The difficulties with the first of these outliers are discussed above. The latter three systems—one semidetached and two detached—are substantially lower than main-sequence expectations by 0.4–0.7 dex, consistent with somewhat evolved secondaries. Three of the four semidetached systems have $\log g_2 < \log g_1$. These semidetached systems, along with the two detached systems with low $\log g_2$, are consistent with Algol-type systems that have undergone mass-ratio reversal and contain secondaries that are larger than main-sequence expectations.

5.3. K22 and the Present Work

Both the contact and the detached K22 solutions to the noncontact systems in our sample proved to be unreliable. Their contact solution to the one contact system was more accurate, but the joint LC–BF solution was able to achieve much greater precision. For the 12 noncontact systems, the joint fit values for $\log q$ have a median uncertainty less than 13% as large as the median uncertainty on $\log q$ in K22. Due to the inability of shallow LCs to distinguish between the effects of low q, low i, and high $l3$, many of the values for q in K22 were significantly in error. On average, we find that the K22 values for q are higher than those here found directly from component velocities. This is a consequence of poorly determined third light in the K22 analysis. Their values for $l3$ for our sample are distributed uniformly from 0 to 1, but only three of these systems actually contain measurable third light (all with $l3 \lesssim 0.3$).

In addition to overestimating $l3$, K22 systematically overestimated $\cos i$ of the detached binaries (underestimated i). Figure 34 shows a comparison between the K22 values for $\cos i$ and the values that the joint fit obtains. Both of these overestimates are largely consequences of K22 fitting contact models to detached binaries. In other words, to fit the shallow minima in the systems' LCs, the contact models of K22 were forced toward larger values for both $l3$ and $\cos i$. This highlights the necessity of knowing a system's geometry when retrieving system parameters—and BFs greatly constrain system geometry.

The presence of LC asymmetries (e.g., spots) compromises the modeling process, resulting in uncertain inclinations that propagate into large uncertainties on component masses. The joint LC–BF solution finds well-constrained primary masses for systems with inclinations above $i \sim 45°$. Below this, they become very uncertain due to the $M \propto (\sin i)^{-3}$ dependence.

From our experience with jointly fitting LCs and BFs, we caution that such solutions are often multimodal, with chi-squared minimum locations that shift depending on the relative weight assigned to the LC data and the BF data. In the absence of additional physical features (e.g., spots), the best-fitting model parameters should be expected to reproduce both the LC and the BF to a level consistent with the noise in each data set, e.g., $\chi^2_\nu \sim 1$.

KIC05802834 showcases the necessity of including reflection effects when fitting the LC of a binary having different temperature components; we were unable to reproduce the LC without the irradiation and reflection effects, which are inherently present in a $T_1 \neq T_2$ system. The contact model of K22 failed to reproduce the breadth of the secondary minimum due to its adherence to a near-equal-temperature

solution. The reflection effects evident in the system place a lower limit on the size of the secondary, despite its nonappearance in the BF, because the secondary must reflect enough light during secondary minimum to reproduce the unequal minima.

6. Conclusions

Our primary goal was to investigate 18 ambiguous-geometry binaries that appeared to have longer periods and higher mass ratios than allowed by models for the evolution and structure of contact binaries with convective envelopes (i.e., W UMa systems). Of these systems, we find that 12 are either detached (eight) or semidetached (four), and five are either rotating (five) or pulsating variables (one). Only one (KIC07766185) turned out to be a contact binary. However, it falls well above the limit of system masses ($M_{\rm tot} < 2.47\,M_{\odot}$, for initial primary masses $M_1 < 1.3\,M_{\odot}$) for which the M22 evolutionary tracks are valid. Therefore, none of the systems in this sample violate the predictions of the M22 evolutionary scenario.

We have demonstrated that jointly fitting models to system LCs and BFs is a powerful way to retrieve system parameters more accurately and precisely than fitting LCs alone. Other than providing a direct measurement of q, BFs also allow for measurements of $l3$ and R_2/R_1, and they include important information about T_2/T_1 and inclination. Combining the information in both the BFs and the LCs allows for determination of the inclination, and therefore, the individual radii and masses of the components.

The secondaries in the 12 noncontact systems are systematically hotter and larger than MS expectations (Figures 33 and 32). Heating of the secondaries by the primaries may be responsible for both these effects. Four of the secondaries appear to fill their Roche lobes, discordant with the standard evolutionary scenario in which the primary is the first to overfill its Roche lobe. These detached systems may have initially come together under the standard scenario but have since undergone mass-ratio reversal, leaving a bloated secondary. Statistics on a set of system and component parameters for such systems will be helpful in constraining evolutionary scenarios for intermediate-mass binaries.

Acknowledgments

We acknowledge helpful conversations with Lawrence A. Molnar regarding the M22 evolutionary models and with Max Moe regarding tertiaries in multiple-star systems. This work was supported by the National Science Foundation through grant AST-2108347. This work has made use of data from the European Space Agency (ESA) mission Gaia (https://www.cosmos.esa.int/gaia), processed by the Gaia Data Processing and Analysis Consortium (DPAC, https://www.cosmos.esa.int/web/gaia/dpac/consortium). Funding for the DPAC has been provided by national institutions, in particular the institutions participating in the Gaia Multilateral Agreement.

Facilities: ARC (ARCES), KEPLER, GAIA.

Software: `astropy` (Astropy Collaboration et al. 2013, 2018), `emcee` (Foreman-Mackey et al. 2013), `IRAF` (Tody 1986, 1993), `jupyter notebook` (Kluyver et al. 2016), `matplotlib` (Hunter 2007), `numpy` (Harris et al. 2020), `PHOEBE` (Prša et al. 2016), `scipy` (Oliphant 2007; Vugrin et al. 2007; Virtanen et al. 2020), `Uncertainties`: a Python package for calculations with uncertainties, Eric O. LEBIGOT, http://pythonhosted.org/uncertainties/.

ORCID iDs

Evan M. Cook https://orcid.org/0000-0003-0983-0273
Henry A. Kobulnicky https://orcid.org/0000-0002-4475-4176

References

Arbutina, B. 2007, MNRAS, 377, 1635
Arbutina, B. 2009, MNRAS, 394, 501
Astropy Collaboration, Price-Whelan, A. M., Sipőcz, B. M., et al. 2018, AJ, 156, 123
Astropy Collaboration, Robitaille, T. P., Tollerud, E. J., et al. 2013, A&A, 558, A33
Balaji, B., Croll, B., Levine, A. M., & Rappaport, S. 2015, MNRAS, 448, 429
Balona, L. A. 2017, MNRAS, 467, 1830
Balona, L. A. 2018, MNRAS, 479, 183
Balona, L. A. 2019, MNRAS, 490, 2112
Barceló Forteza, S., Roca Cortés, T., & García, R. A. 2018, A&A, 614, A46
Binnendijk, L. 1970, VA, 12, 217
Bonnell, I. A., & Bate, M. R. 2005, MNRAS, 362, 915
Brown, T. M., Latham, D. W., Everett, M. E., & Esquerdo, G. A. 2011, AJ, 142, 112
Cannon, A. J., & Pickering, E. C. 1993, yCat, III/135A
Casagrande, L., Schönrich, R., Asplund, M., et al. 2011, A&A, 530, A138
Castelli, F., & Kurucz, R. L. 2003, in IAU Symp. Proc. 210, Modelling of Stellar Atmospheres, ed. N. Piskunov, W. W. Weiss, & D. F. Gray (San Francisco, CA: ASP), A20
Chini, R., Hoffmeister, V. H., Nasseri, A., Stahl, O., & Zinnecker, H. 2012, MNRAS, 424, 1925
Coughlin, J. L., López-Morales, M., Harrison, T. E., Ule, N., & Hoffman, D. I. 2011, AJ, 141, 78
Darwin, G. H. 1879, Obs, 3, 79
Ding, X., Ji, K.-F., & Li, X.-Z. 2021, PASJ, 73, 786
Duquennoy, A., & Mayor, M. 1991, A&A, 248, 485
Eggleton, P. P. 2012, JASS, 29, 145
Fabrycky, D., & Tremaine, S. 2007, ApJ, 669, 1298
Flannery, B. P. 1976, ApJ, 205, 217
Foreman-Mackey, D., Hogg, D. W., Lang, D., & Goodman, J. 2013, PASP, 125, 306
Frasca, A., Molenda-Żakowicz, J., De Cat, P., et al. 2016, A&A, 594, A39
Gaia Collaboration 2022, yCat, I/358
Gaia Collaboration, Vallenari, A., Brown, A. G. A., et al. 2023, A&A, 674, A1
Gaulme, P., & Guzik, J. A. 2019, A&A, 630, A106
Gazeas, K., & Stępień, K. 2008, MNRAS, 390, 1577
Gray, D. F. 2005, The Observation and Analysis of Stellar Photospheres (Cambridge: Cambridge Univ. Press)
Harris, C. R., Millman, K. J., van der Walt, S. J., et al. 2020, Natur, 585, 357
Horvat, M., Conroy, K. E., Jones, D., & Prša, A. 2019, ApJS, 240, 36
Huang, S.-S. 1966, AnAp, 29, 331
Hunter, J. D. 2007, CSE, 9, 90
Hut, P. 1981, A&A, 99, 126
Jiang, D., Han, Z., Ge, H., Yang, L., & Li, L. 2012, MNRAS, 421, 2769
Jiang, D., Han, Z., & Li, L. 2014, MNRAS, 438, 859
Kirk, B., Conroy, K., Prša, A., et al. 2016, AJ, 151, 68
Kiseleva, L. G., Eggleton, P. P., & Mikkola, S. 1998, MNRAS, 300, 292
Kluyver, T., Ragan-Kelley, B., Pérez, F., et al. 2016, in Positioning and Power in Academic Publishing: Players, Agents and Agendas, ed. F. Loizides & B. Schmidt (Amsterdam: IOS Press), 87
Kobulnicky, H. A., Molnar, L. A., Cook, E. M., & Henderson, L. E. 2022, ApJS, 262, 12
Kuiper, G. P. 1941, ApJ, 93, 133
Latković, O., Čeki, A., & Lazarević, S. 2021, ApJS, 254, 10
Li, L., & Zhang, F. 2006, MNRAS, 369, 2001
Lucy, L. B. 1968, ApJ, 151, 1123
Macrae, D. A. 1952, ApJ, 116, 592
Molnar, L., Avery, A., Blain, M., et al. 2022, AAS Meeting Abstracts, 54, 308.01
Muller, G., & Kempf, P. 1903, ApJ, 17, 201
Nielsen, M. B., Gizon, L., Schunker, H., & Karoff, C. 2013, A&A, 557, L10

Nordström, B., Mayor, M., Andersen, J., et al. 2004, A&A, 418, 989
Oliphant, T. E. 2007, CSE, 9, 10
Paxton, B., Bildsten, L., Dotter, A., et al. 2011, ApJS, 192, 3
Pecaut, M. J., & Mamajek, E. E. 2013, ApJS, 208, 9
Pešta, M., & Pejcha, O. 2022, arXiv:2212.02553
Prša, A. 2018, Modeling and Analysis of Eclipsing Binary Stars; The Theory and Design Principles of PHOEBE (Bristol: IOP Publishing)
Prša, A., Batalha, N., Slawson, R. W., et al. 2011, AJ, 141, 83
Prša, A., Conroy, K. E., Horvat, M., et al. 2016, ApJS, 227, 29
Qian, S. B., Zhang, J., He, J. J., et al. 2018, ApJS, 235, 5
Raghavan, D., McAlister, H. A., Henry, T. J., et al. 2010, ApJS, 190, 1
Ramírez-Preciado, V. G., Roman-Lopes, A., Román-Zúñiga, C. G., et al. 2020, ApJ, 894, 5
Rasio, F. A. 1995, ApJL, 444, L41
Reid, I. N., & Gizis, J. E. 1997, AJ, 113, 2246
Reinhold, T., Reiners, A., & Basri, G. 2013, A&A, 560, A4
Rucinski, S. 1999, in ASP Conf. Ser. 185, IAU Coll. 170: Precise Stellar Radial Velocities, ed. J. B. Hearnshaw & C. D. Scarfe (San Francisco, CA: ASP), 82
Rucinski, S. M. 1992, AJ, 104, 1968
Rucinski, S. M. 2006, MNRAS, 368, 1319
Schatzman, E. 1962, AnAp, 25, 18
Shapley, H. 1948, HarMo, 7, 249
Soubiran, C., Jasniewicz, G., Chemin, L., et al. 2018, A&A, 616, A7
Tody, D. 1986, Proc. SPIE, 627, 733
Tody, D. 1993, in ASP Conf. Ser. 52, Astronomical Data Analysis Software and Systems II, ed. R. J. Hanisch, R. J. V. Brissenden, & J. Barnes (San Francisco, CA: ASP), 173
Tokovinin, A., & Moe, M. 2020, MNRAS, 491, 5158
Tran, K., Levine, A., Rappaport, S., et al. 2013, ApJ, 774, 81
Tylenda, R., Hajduk, M., Kamiński, T., et al. 2011, A&A, 528, A114
Virtanen, P., Gommers, R., Oliphant, T. E., et al. 2020, NatMe, 17, 261
Vugrin, K. W., Swiler, L. P., Roberts, R. M., Stucky-Mack, N. J., & Sullivan, S. P. 2007, WRR, 43, W03423
Wadhwa, S. S., De Horta, A., Filipović, M. D., et al. 2021, MNRAS, 501, 229
Wang, S.-i., Hildebrand, R. H., Hobbs, L. M., et al. 2003, Proc. SPIE, 4841, 1145
Webbink, R. F. 1976, ApJ, 209, 829
Yakut, K., & Eggleton, P. P. 2005, ApJ, 629, 1055
Zhang, J., Qian, S.-B., Wu, Y., & Zhou, X. 2019, ApJS, 244, 43